Technische Universität Braunschweig

DLR Institut für Raumfahrtsysteme

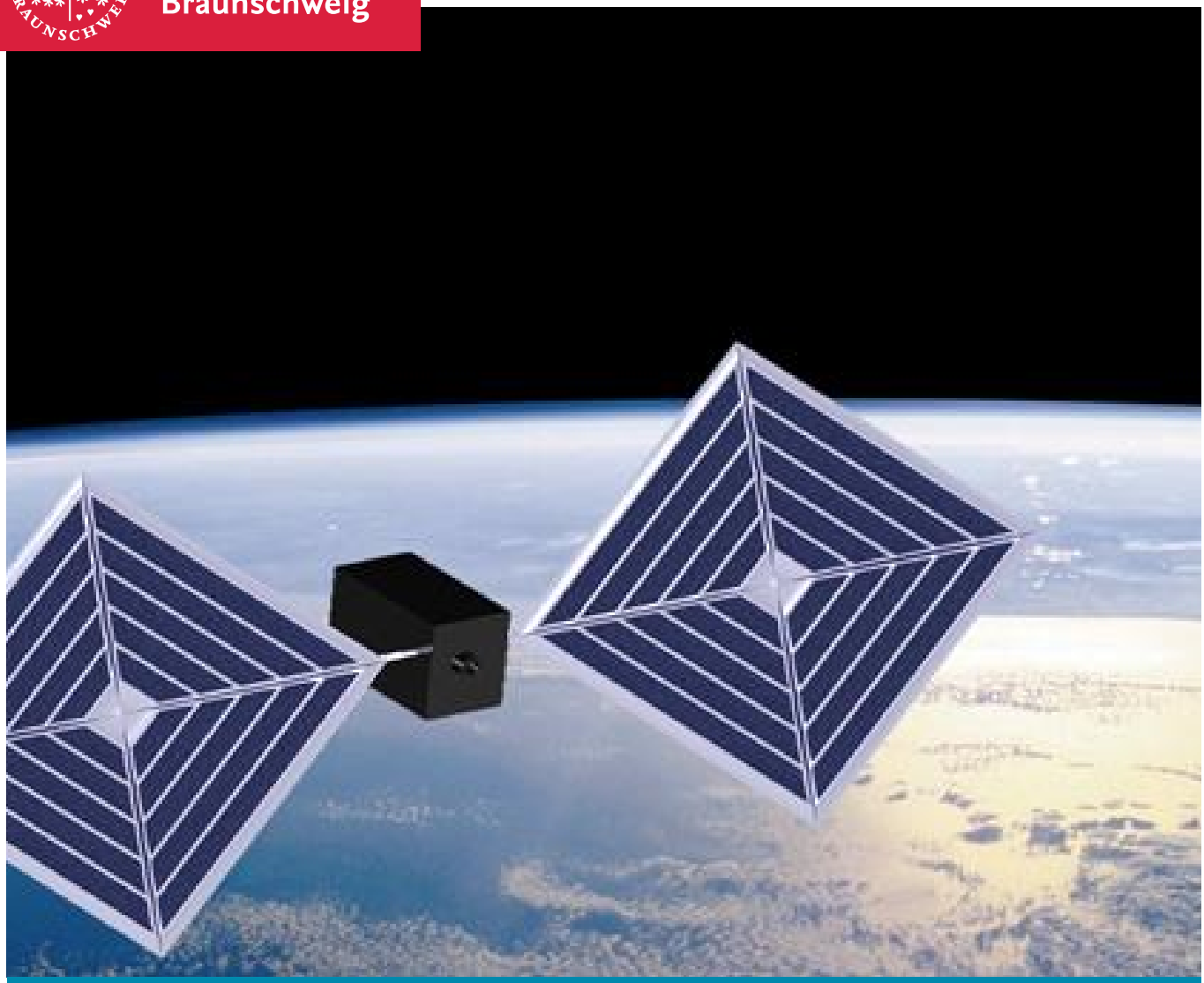

R XXXX X (beim Betreuer beantragen!) Mechanical analysis and accommodation study of the gossamer solar array GoSolAr

Institut für Raumfahrtsysteme

Niklas Bildt

September 11, 2017

Aufgabenstellung

Die Originalaufgabenstellung ist bei Studienarbeiten dem ungebundenen Institutsexemplar beizufügen, bei Bachelor-, Master- und Diplomarbeiten dem gebundenen Exemplar zur Vorlage bei der Fakultät. Die Aufgabenstellung bei Bachelor-, Master- und Diplomarbeiten wird vom Fachbereich ausgegeben (bei CSE-Masterarbeit vom CSE Office), dieser registriert den Beginn und die Abgabe der Arbeit und stempelt diese Angaben auf das letzte Blatt der Original-Aufgabenstellung.

Eine Diplom-, Studien-, Bachelor- bzw. Masterarbeit soll zeigen, dass man in der Lage ist, in begrenzter Frist eine Aufgabe nach wissenschaftlichen Methoden selbständig zu bearbeiten.

Die Aufgabenstellung kann Literaturhinweise enthalten, die als Einstieg in die Aufgabe gedacht sind. Es wird erwartet, daß weitere Literatur selbständig gesammelt wird (Bibliotheken der TU, des Instituts, etc.).

Wichtig: Schriftverkehr mit Dritten bei Nennung des die Arbeit betreuenden Instituts bedarf der vorherigen Genehmigung.

In der Abgabeversion dann dieses Blatt entfernen und an dieser Stelle durch die Aufgabenstellung ersetzen!

Eidesstattliche Erklärung

Ich erkläre hiermit an Eides Statt, dass ich die nachfolgende Arbeit selbständig und nur unter Zuhilfenahme der angegebenen Literatur angefertigt habe.

_____

Datum, Unterschrift

Abstract

Die Übersicht enthält kurz gefasste Angaben über die Zielsetzung, die angewandten Methoden und die gewonnenen Ergebnisse. Sie soll das Wesentliche aus dem Inhalt der Arbeit in wenigen Sätzen zusammenfassen und ist der eigentlichen Arbeit voranzustellen (höchstens 1/2 bis 1 Seite). Sie soll also nicht lediglich die Aufgabenstellung wiedergeben.

Contents

1 Introduction

1.1 Aims of the work

This study thesis is part of a feasability study for a large gossamer solar array of a size of 20 x 20 m^2. A technology demonstrator of 5 x 5 m^2 in size is to be built for an in orbit demonstration. Preparations for the developement are done within this study thesis. The response of the PV array due to a pre tensioning force on the masts is to be examined. Furhter the vibration behaviour depending on the mast type, especially its stiffness and the pre tensioning force shall be examined. Favourable options for these parameters shall be found. Additionally the behaviour of the array under static loads is to be examined. In an accommodation study the approximate sizes and efficiencies of several options using different components and arrangements for the GoSolAr shall be investigated. The aim is to see how the GoSolAr can be accommodated on a S/C and fit in the payload fairing of a L/V.

1.2 Approach

In chapter 2 the theoretical basics are elaborated. Basic information on launch vehicles are given, the theory behind FEA is examined, loads on the PV array are determined and the current design status of the technology demonstrator is described. In chapter 3 the procedure of the FEA is described. The model is created in ANSYS workbench, materials and material properties are elaborated and and precedent calculations are done. The approach for the FEA is shown and the results are evaluated. chapter 4 shows how the accommodation study is done. The approach as well as the outcomes are shown and the outcomes are evaluated. chapter **??** summarises the results of the study thesis. chapter **??** keine ahnung and chapter **??** shows future prospects for the GoSolAr project.

2 State of the art review

2.1 Launch vehicles

In preparation for the accommodation study applicable launch vehicles (L/V) are examined. In the following the European L/Vs Ariane 5 and Vega are considered in more detail. Particular attention will be paid to the available space in the payload fairing which is the most important restriction regarding the accommodation of the GoSolAr on a spacecraft.

2.1.1 Ariane 5

Ariane 5 is a heavy-lift launch vehicle. It is primarily utilised for delivery of heavy weight spacecraft to the low earth orbit (LEO) and geostationary transfer orbit (GTO). The Ariane 5 ES can carry a payload of 20 t to the LEO which is vital for the $(5\ m)^2$ technology demonstrator that is to be tested in the LEO. The Ariane 5 ECA is capable of delivering up to 9,700 kg to the GTO which is critical e.g. for the future application of the GOSolAr on a satellite.

Propulsion

The Cryogenic main core stage of the Ariane 5 is powered by a Vulcain 2 engine which creates 1390 kN of thrust in the vacuum. The main stage has a combustion time of 540 s using 170 t of liquid oxygen and liquid hydrogen. The solid rocket boosters are driven by a solid propellant motor delivering a mean of 7000 kN of thrust for 130 s. 240 t of solid propellant per booster are used for that. The cryogenic upper stage accommodates a HM7B engine fed by 14.9 t of liquid hydrogen and liquid oxygen. It generates a thrust of 67 kN for 945 s.

Payload fairing

The payload fairing is made up of two carbon fiber half shells. Its external diameter is 5.4 m. The fairing has a horizontal and a vertical separation system which work pyrotechnically. The space in the payload fairing is the most important property of the L/V regarding the accommodation study. The usable volume in the fairing is called the static volume. It sets the limit for the dimensions of the S/C. Additionally things like manufacturing tolerances or displacement of the S/C due to loads need to be considered when designing or in this case doing the accommodation study. So, sufficient clearances need to be considered. The payload fairing has an outer diameter of 5.4 m while the usable inside diameter is between 4480 mm and 4570 mm. The usable height with this diameter is 10039 mm. The total height of the fairing is 15589 mm. The further dimensions can be seen in figure 2.1. Another scenario that is taken into account is the dual launch configuration. The SLYDA 5 carrying structure is a cylindrical carbon structure which is mounted above the first S/C. On top of the SYLDA 5 the second S/C is mounted. The SYLDA can bee seen in figure 2.2 The SYLDA is also separated by pyrotechnical means and pushed away by springs. If the S/C is stored underneath the SYLDA 5 carrying structure there is a usable diameter of 4000 mm and a usable height that can vary from 2829 mm to 4929 mm. If stored above the SYLDA 5 the usable diameter is still 4480 mm but

the completely usable height varies from 3649 mm to 5749 mm depending on the configuration. All dimensions can be seen in figure 2.1.

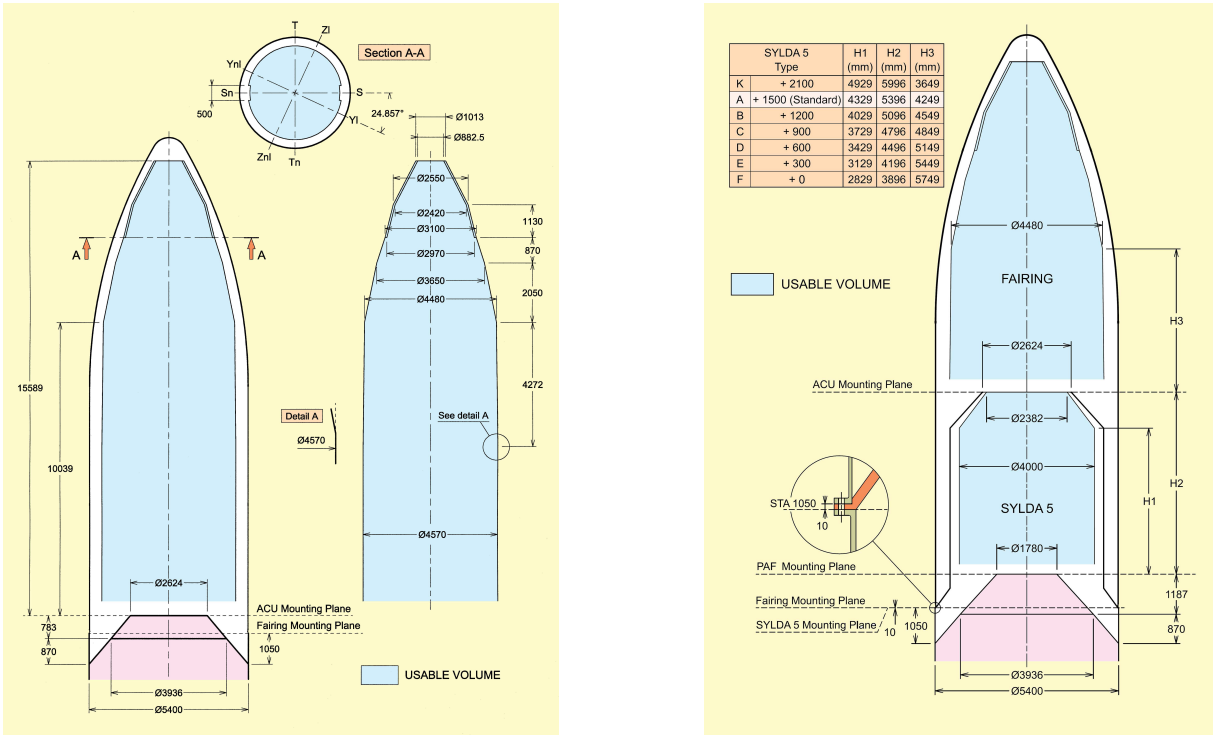

Figure 2.1: Payload fairing of the Ariane 5 without and with SYLDA(Arianespace, 2016).

Typical GTO mission sequence

First the cryogenic core stages engine is ignited. If the on-board registers the good functioning of the engine, 6.05 s after the ignition the lift-off is commenced by the ignition of the boosters. When an accelerometer realizes the boosters are burnt they are released. About one minute later, the fairing is separated when the aerothermal flux comes below a threshold value which is 1135 $\frac{W}{m^2}$ for GTO missions. In the proximity of the targeted orbit the main stage engine is cut off and 6 seconds later the main staged is dropped. A ventilation hole in the main stages hydrogen tank makes it spin and ensures a re-entry and splashdown. Shortly after the release of the main stage the upper stage is ignited. It provides thrust until the reaching of the final targeted orbit is perceived and it is then shut down. 2 seconds after that, the S/C is released. The whole launch procedure is visualized in figure 2.3.

Ariane 5 ES ATV

Due to the ATV being considered as a reference S/C for this work the special version of the Ariane 5, the Ariane 5 ES ATV needs to be examined. The Ariane 5 ES ATV was developed for the launch of the ATV. The main differences are the main stage with an improved Vulcain 2 engine and a reignitable upper stage. The upper stage is ignited three times during an ATV mission. (Arianespace, 2016) (ESA-homepage, n.d.a) (ESA-homepage, n.d.b)

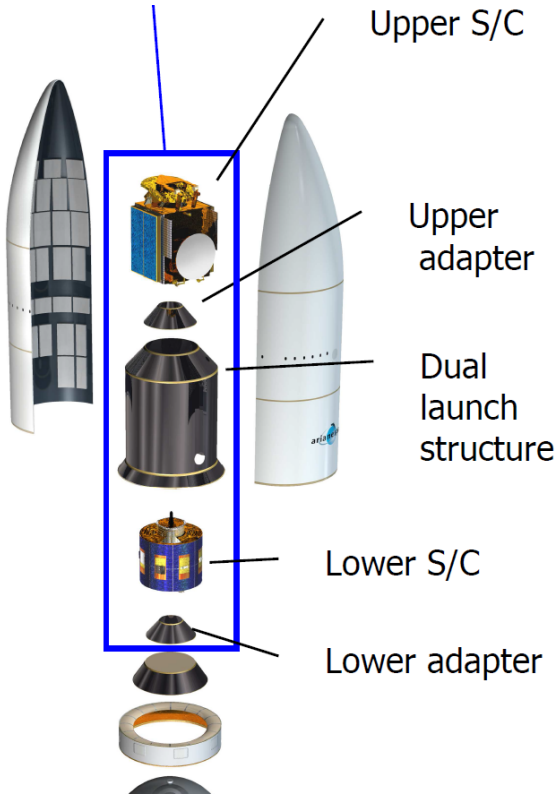

Figure 2.2: Exploded view of Ariane 5 with SYLDA(Arianespace, 2016).

2.1.2 Vega

Vega is a L/V for small to midsize payloads. It is designed to deliver payloads to near earth orbits. It is able to carry a maximum payload of 1500 kg to a 700 km circular orbit. Its first launch was in 2012.

Propulsion & mission sequence

Vega is a four stage rocket composed of 3 engines powered by solid propellant and one stage that is uses liquid propellant. The P80 first stage is powered by 87,710 kg Hydroxyl-Terminated Poly Butadiene (HTPB) 1912 which is a solid propellant. The Solid Rocket Motor (SRM) generates 3,015 kN of thrust in a vacuum for 113 s. The stage is released at an altitude of approximately 58 km. The diameter of the P80 first stage is the same as Ariane 5's boosters diameter and the length is also similar. The reason for that is that the boosters of Ariane 5 were the basis for the development of the P80 first stage. The Zefiro solid rocket motor is used for the second and third stage. It also uses HTPB 1912 as a solid propellant. The Zefiro has a flexible nozzle with electromechanical actuators so the thrust can be directed. The so called Z23 second stage and Z9 third stage differ in length thus they differ in propellant capacity and they also differ in maximum thrust. The Z23 second stage contains 23,814 kg of propellant and runs for about 78 s with a maximum thrust of 1,120 kN in vacuum. The Z9 third stage delivers a maximum thrust of 317 kN for around 120 s using 10,567 kg of solid propellant. The last stage is the Attitude & Vernier Upper Module (AVUM). The AVUM is able to inject payloads into the desired orbit and provides fine positioning. It consists

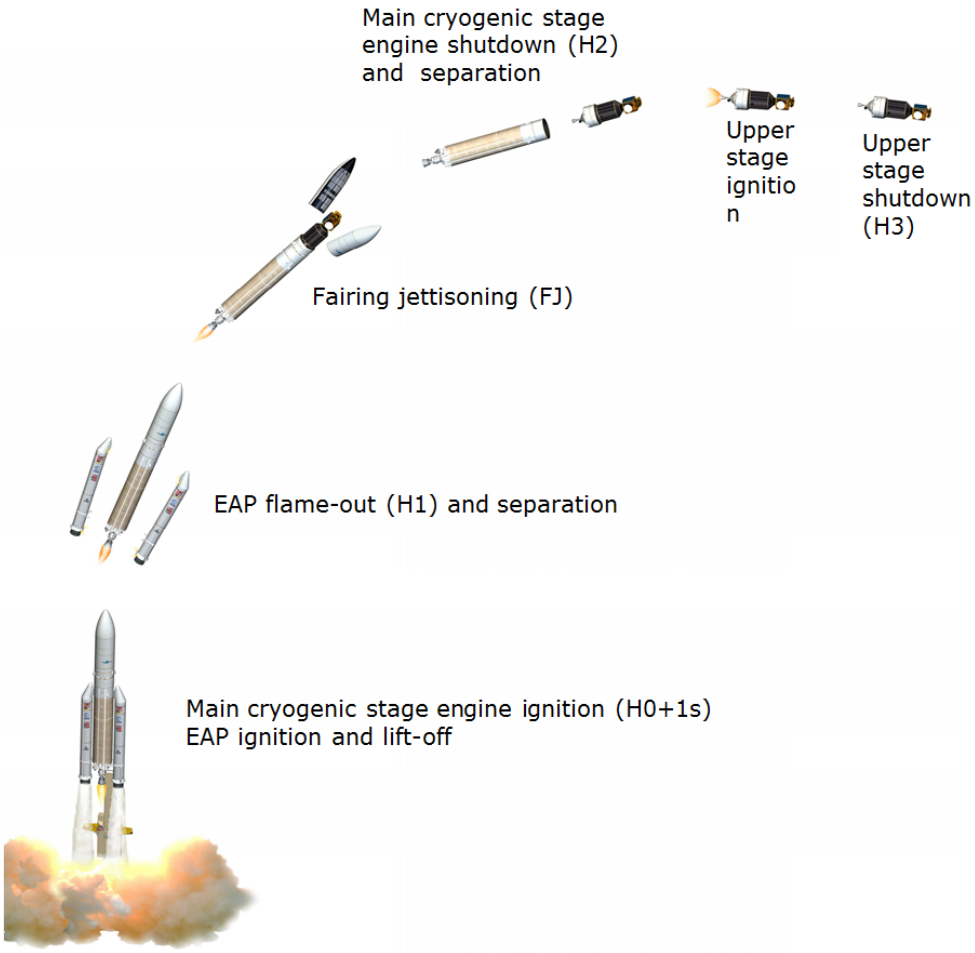

Figure 2.3: Ariane 5 mission sequence(Arianespace, 2016).

of a bipropellant main propulsion system and a monopropellant propulsion system. The Main system is powered by 577 kg of the liquid propellant Unsymmetrical Dimethylhydrazine (UDMH) and Nitrogen Tetroxide (NTO). The engine delivers 2.45 kN thrust in vacuum. The monopropellant propulsion system consists of two sets of three thrusters and is powered by 38.6 kg of hydrazine. The main propulsion is used for orbital injection and the monopropellant system is needed to control attitude and roll. The AVUM is restartable up to five times. The first three stages are responsible for setting the spacecraft to sub-orbital flight. After the ignition of the third stage, the payload fairing is jettisoned when the aerothermal flux reaches a value below 1135 $\frac{W}{m^2}$. After the third stage is cut off the AVUM is used for orbital maneuvers during the ballistic phase. Usually the AVUM burns two times. The first one is done to direct into a desired intermediate orbit and the second one to get into the final orbit. When in the final orbit the S/C is released. As written before the AVUM is capable of up to five burns. That allows Vega to deliver different S/C to different orbits in a multiple launch configuration. The mission sequence is visualized in figure 2.4.

Payload fairing

Similar to the fairing of Ariane 5 the payload fairing of Vega is composed of two half shells which split vertically in the middle by pyrotechnic means. It is separated from the AVUM by a horizontal

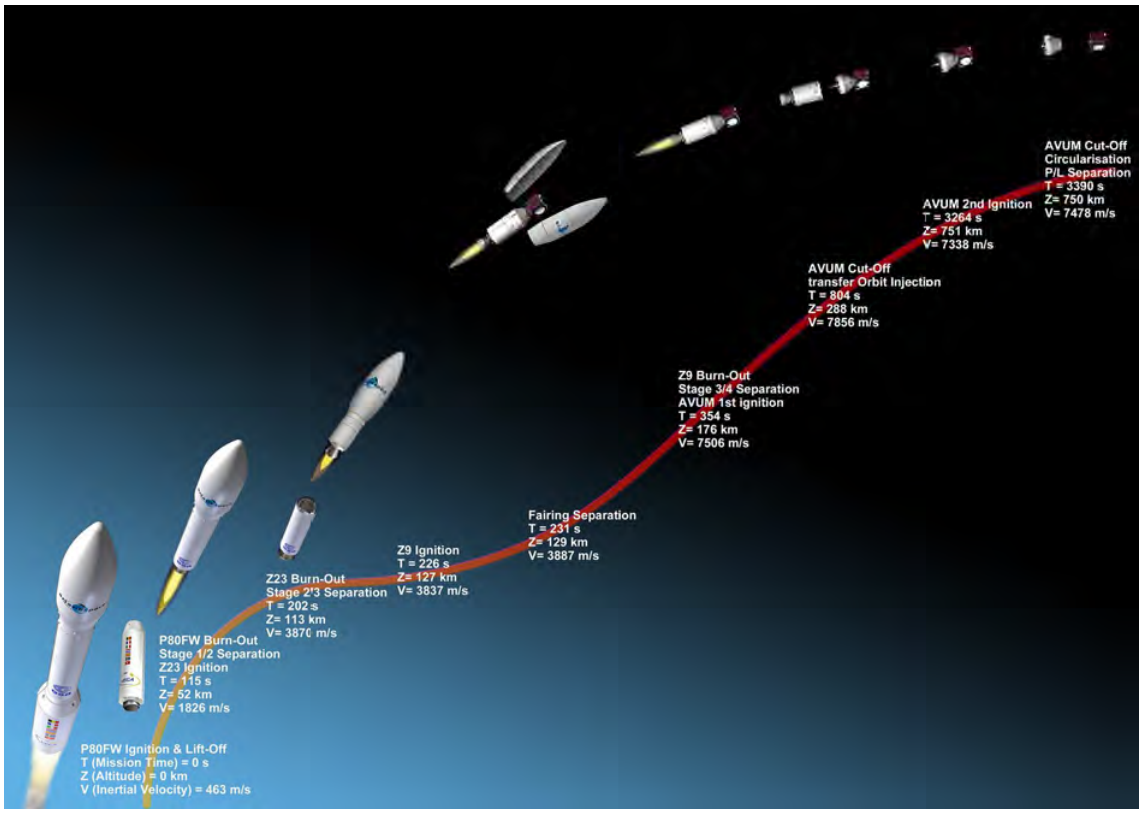

Figure 2.4: Vega mission sequence(Arianespace, 2014).

interface. Dimensions The payload fairing provides an inner diameter between 2,363 mm and 2,307 mm in the quasi cylindrical area over a length of 3,180 mm. But the space is limited by notches which partly reduce the usable diameter to 2,216 mm. It is shown in figure 2.5. There is also a version available with extended length. The length of the quasi cylindrical part of this version is 3,569.5 mm. The detailed dimensions are visualized in figure 2.5. For a multiple launch configuration the Vega Secondary Payload Adapter (VESPA) can be used. There are two versions of it. A small version that offers a nearly cylindrical space with a diameter of approximately 1820 mm and a height of 1000 mm. The larger version has a slightly conical shape and offers an extended height of 1500 mm but a smaller diameter of about 1775 mm. They can be seen in figure 2.6.

(Arianespace, 2014)

2.2 Reference missions & mission requirements

In order to determine and estimate the operating conditions, especially the occurring loads on the solar array it is necessary consider reference missions. This includes reference S/C such as the Automatic Transfer Vehicle (ATV) and applicable electric thrusters such as the High Power Electric Propulsion Program (HiPEP). The considered loads are the athmospheric drag and the solar radiation pressure.

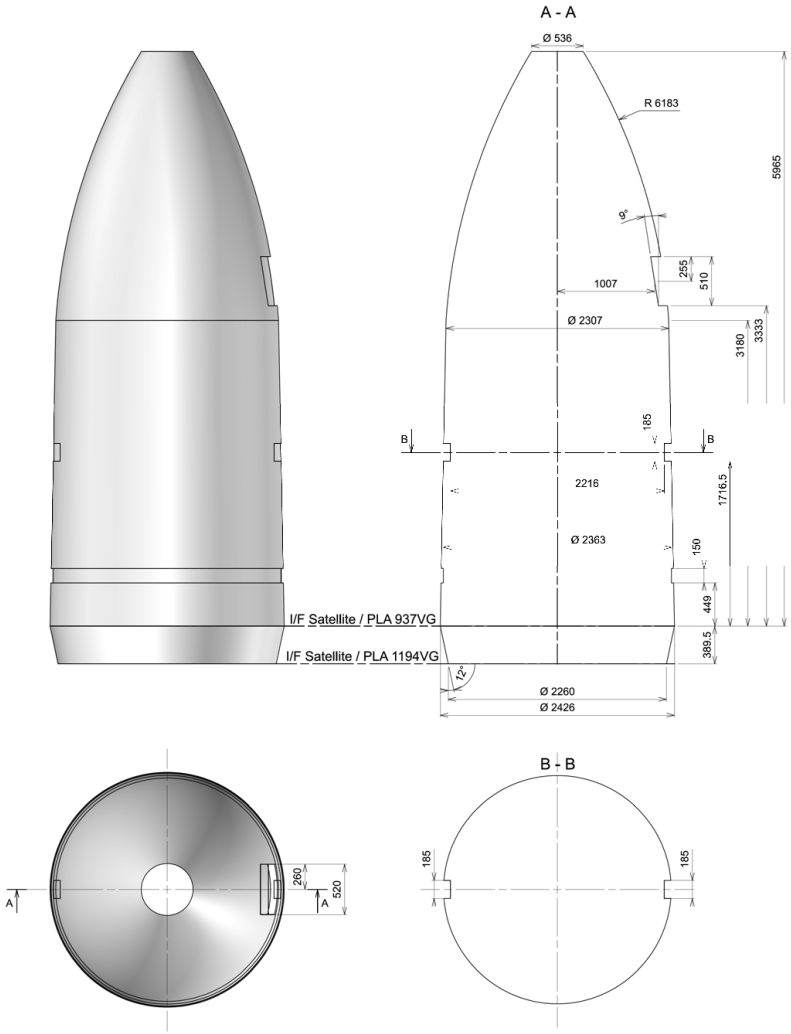

Figure 2.5: Vega payload fairing(Arianespace, 2014).

2.2.1 Electric propulsion

Due to the fact that the GoSolAr is supposed to generate electricity to drive an electrically powered propulsion system on a S/C the HiPEP is examined in more detail to obtain knowledge about the order of magnitude in which current electric propulsion systems work. First the basic functioning of an ion thruster is explained. Afterwards the technical data of the HiPEP which is usable for the FE analysis is stated.

Functional principle of an ion thruster

The ion thruster propulsion system is mainly consisting of a discharge chamber with a discharge cathode on one side and two grids, the positively charged screen grid and the negatively charged acceleration grid, on the other side as shown in figure 2.7. Behind the grids the neutralizer is located. The propellant is injected into the chamber and electrons are emitted from the cathode using the process of thermionic emission. The propellant is ionized removing electrons. The ionization is achieved by electron bombardment. Colliding with a propellant atom the electron releases further

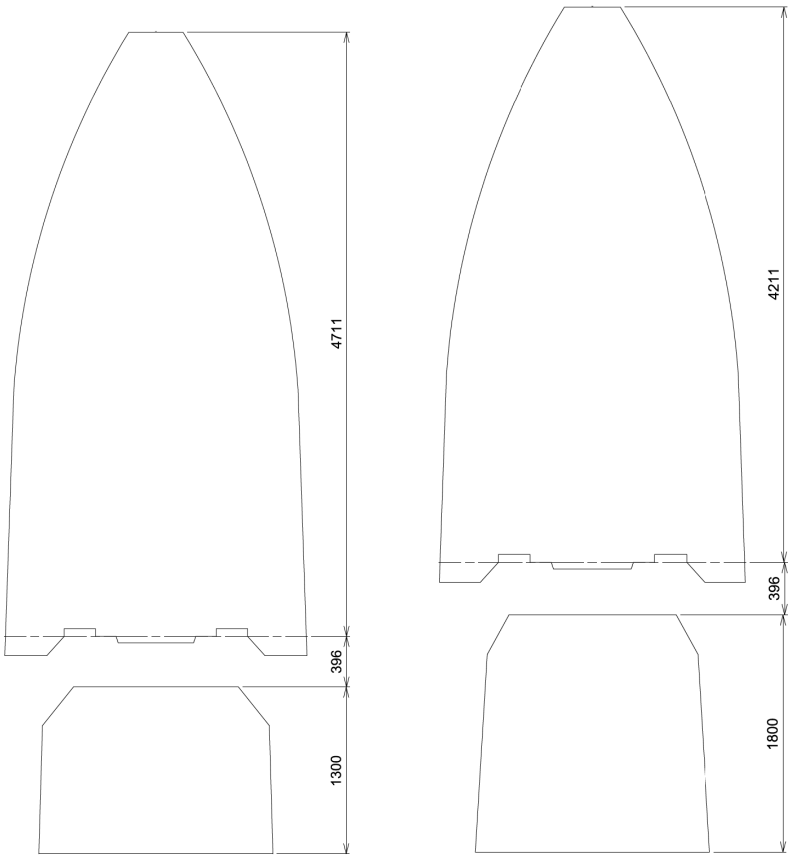

Figure 2.6: Vega payload fairings with VESPA(Arianespace, 2014).

electrons from the propellant atom. The propellant atoms are positively charged. The positive charge of the propellant ions and the negative charge of the free electrons are in balance. This macroscopically uncharged gas is called plasma. The electrons emitted by the discharge cathode are attracted to the positively charged walls of the chamber. On their way from the cathode to the walls the electrons collide with the gas atoms. The electrons are prevented to reach the chamber walls by strong magnets keeping them in the chamber for a longer duration which increases the chance of a collision. The ions are moving towards the grids due to diffusion. When reaching the grids the ions are accelerated due to the potential difference from the positive screen grid to the negative acceleration grid. The ions are reaching velocities up to 40 $\frac{\text{km}}{\text{s}}$. The neutralizer neutralizes the ion beam by adding electrons to prevent it from travelling back to the spacecraft. The neutralizer is necessary because if it were not present the S/C would be negatively charged emitting a positively charged ion beam. The ion beam would decelerate due to the attractive fore between ion beam and S/C. (NASA-homepage, 2016)

The High Power Electric Propulsion Program (HiPEP) Ion Thruster

In 2002 the NASA initiated the development of a high-power electric propulsion for the Jupiter Icy Moon Orbiter. The HiPEP was developed by NASA Glenn Research Center (GRC). It is an 20 – 50 kW ion thruster which is the order of magnitude of the GoSolAr. Its specific impulse is 6000 – 9000 s exceeding a propellant throughput capacity of 100 $\frac{\text{kg}}{\text{kW}}$. It uses Xenon as the propellant.

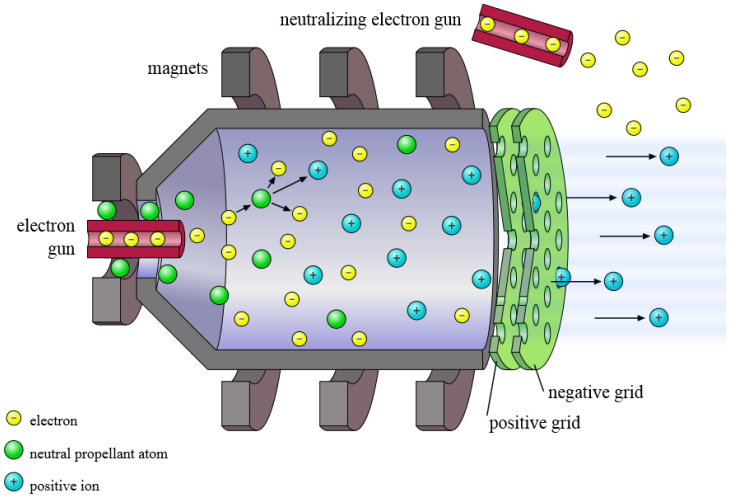

Figure 2.7: Schematic structure of an ion thruster(Anthony, 2012).

The maximum thrust of the HiPEP is 670 mN. (Foster et al., 2004) This value can be used for the FE analysis simulating the occurring forces when the S/C is accelerated by an electric propulsion system.

2.2.2 Automated Transfer Vehicle (ATV)

The ATV is examined because it is planned to use the GoSolAr on a spaceship of the scale of the ATV. The ATV is an unmanned S/C that delivered freight to the International Space Station (ISS). Once it is docked to the ISS it is also used to lift the orbit of the ISS. It remains at the ISS for up to 6 months. It is filled with waste from the ISS before it is separated and burnt during the re-entry. The ATV is capable of performing the rendezvous and docking with the ISS as well as departure and deorbitation manoeuvres completely autonomously. The ATV is launched by a special version of the Ariane 5, the Ariane 5 ES ATV. It is approximately 10 m long and 4.5 m in diameter. The mass of the fully loaded ATV is around 20 t while the payload capacity is about 6 t. A value that is important for this work is the docking velocity of 0.071 $\frac{\mathrm{m}}{\mathrm{s}}$. This velocity and mass can be used to simulate the docking impulse on the solar array. The dimensions of the ATV are necessary for the accommodation study. (DLR-homepage, 2017)

2.2.3 Loads

Atmospheric drag

In a LEO the atmospheric drag is a considerable load that acts on the solar array. It is due to residual atmosphere in the LEO that applies a drag pressure p_D on the array that can be determined by the drag equation:

$$p_D = c_D \cdot \frac{1}{2} \cdot \rho \cdot v_a^2 \tag{2.1}$$

Rho is the density of the residual atmosphere, v_a is the velocity of the S/C, and c_D is the drag coefficient. In this case the Newtonian flow theory can be applied because this is a hypersonic molecular

flow. The Newtonian flow theory describes c_D as:

$$c_D = c_p \cdot \sin(\alpha_a) \tag{2.2}$$

with α_a being the inclination to the flow and the pressure coefficient c_p being:

$$c_p = 2 \cdot \sin^2(\alpha_a) \tag{2.3}$$

The solar array is assumed to be perpendicular to the stream, meaning α_a is 90°. So the drag pressure can be calculated as follows:

$$p_D = \rho \cdot v_a^2 \tag{2.4}$$

The velocity va is assumed to be identical to the orbit velocity assuming an orbit with an inclination of 90°. Hence, va is determined as follows:

$$v_a = \sqrt{\mu \cdot \frac{2}{r_0} - \frac{1}{a}} \tag{2.5}$$

The drag pressure is plotted over the orbits radius. The graph is shown in figure 2.8. Based on the operating conditions which include orbit with radii of XXXX drag pressure values of XXXX will be used in the FE analysis.

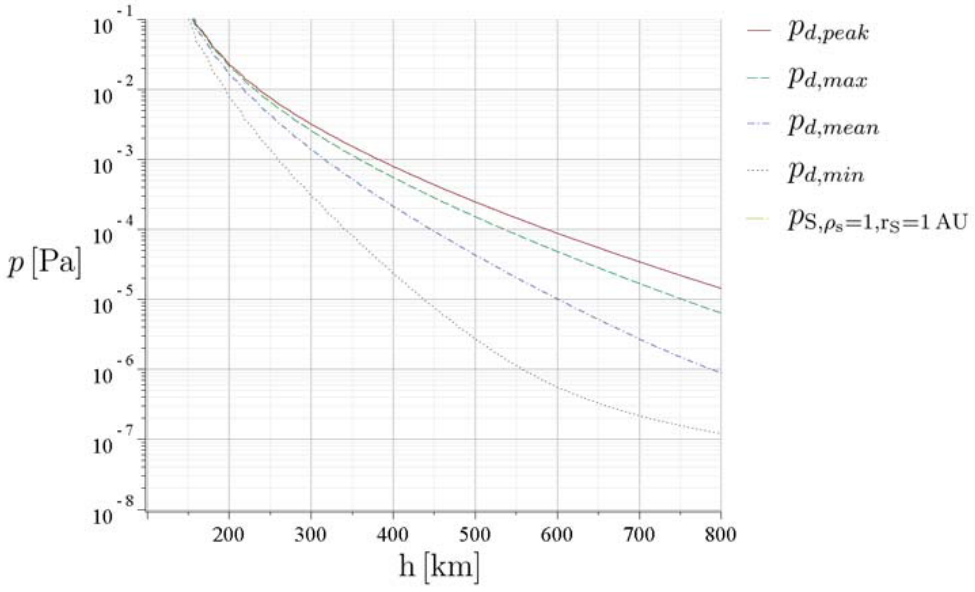

Figure 2.8: The drag pressure over orbit radius(Seefeldt, 2017).

Solar radiation pressure

Due to the large size of the photovoltaic array the solar radiation pressure is a considerable load. An electromagnetic wave always carries an impulse P. The impulse of an electromagnetic wave is defined as:

$$P = \frac{W}{c_l} \tag{2.6}$$

with W being the energy of the wave. The intensity of the wave results from the energy per unit of time and area. The intensity of the wave divided by the speed of light c_l is the impulse per unit of time and area. An impulse divided by time results in a force and a force divided by area results in a pressure. Hence the intensity I divided by c_l is a pressure called solar radiation pressure. The solar radiation pressure is defined as:

$$p_s = \frac{I}{c_l} \tag{2.7}$$

Applying the solar constant E_0 to this equation results in the solar radiation pressure that the solar array is exposed to in the proximity of the earth:

$$p_s = \frac{E_0}{c_l} \tag{2.8}$$

$$p_s = \frac{1367 \frac{W}{m^2}}{299,792,458 \frac{m}{s}} \tag{2.9}$$

$$p_s = 4.56 \cdot 10^{-}6 \frac{N}{m^2} \tag{2.10}$$

This value applies to an absorbed radiation. If the radiation is reflected the pressure on the radiated surface is twice as high as the solar radiation pressure. Thus a maximum pressure of

$$p_s = 9.12 \cdot 10^{-}6 \frac{N}{m^2} \tag{2.11}$$

is acting on the surface.(Tipler, 2000) This value can be used in the FE analysis.

2.3 Mechanical analysis methods

2.3.1 Finite element analysis

Basics of the finite element method

If a part is to be analysed but its shape is too complex to perform analytical calculations the finite element method (FEM) can be used. The basic idea behind FEM is to divide the part in single elements which can be computed quite easily. These elements are connected to each other by their nodes. These nodes are sited on the vertices of the elements and there can also be additional nodes on the edges of the elements. For example in case of a so-called linear 2D element as visible in figure 2.9 there are 4 nodes, one situated on each vertex. In case of a quadratic 3D element there are 8 nodes. On each vertex and on each edge a node is situated. The mechanical behaviour of each node can be described with equation 2.12:

$$k \cdot u = F \tag{2.12}$$

Due to each element having two degrees of freedom, each element has two unknown displacements v and u. In case of the linear element which has 4 nodes this results in 8 equations with 8 unknowns. The resulting system of equations contains a 8 x 8 matrix, called stiffness matrix. These stiffness matrices are solved numerically by the FE software. As a result the displacements off all nodes are known. With the Young's modulus and the displacements the tensions in the elements can be determined.

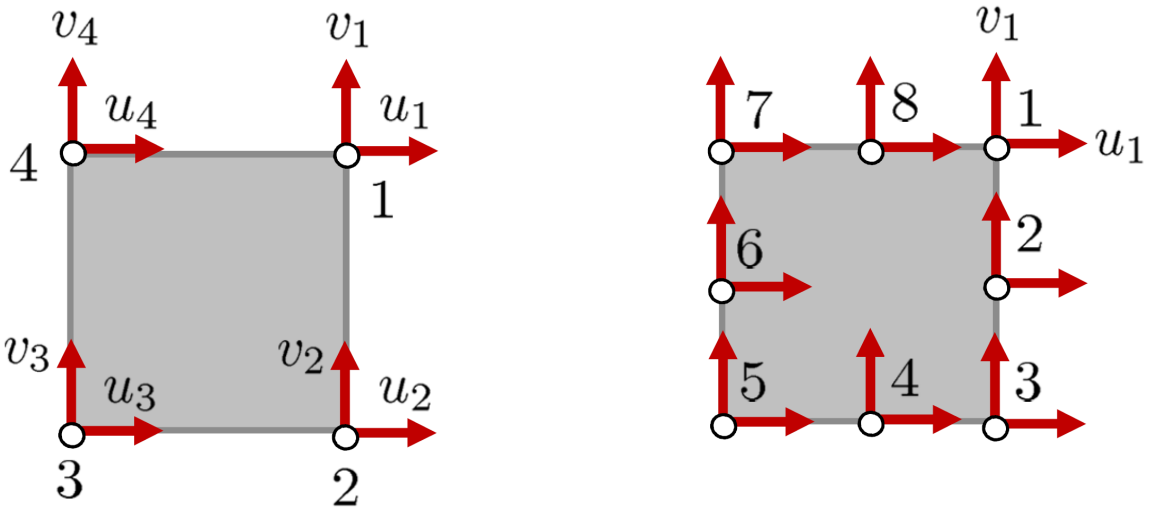

Figure 2.9: Linear and quadratic 3D elements(Bl and Bolea Albero, 2016).

The solvers

For non-linear problem such as the GoSolAr there are two different kinds of solvers, implicit and explicit ones. In both techniques the load is applied incrementally over several time steps. The functioning of the implicit solver is based on the following equation 2.13 for the time t_{n+1}:

$$k_{n+1} \cdot u_{n+1} = F_{n+1} \tag{2.13}$$

The stiffness matrix as well as the displacement are unknown and therefore need to be determined iteratively because the stiffness matrix depends on the displacement by solving the force equilibrium. Using the initial stiffness matrix k_0 the force equilibrium is solved and the displacement u0 is determined. Based on the deformed shape a new stiffness matrix is determined and the fore equilibrium is solved again. This is done until there is no more significant change in u. This process is called the Newton-Raphson method. The Newton-Raphson method is visualized in figure 2.10. The stiffness thus the slope of the red graph changes with each iteration step. This is done until the difference between the applied force and the reaction force, called residual, is below a certain tolerance. After the time step converged the next time step starts. The force is increased and the iteration starts over. The implicit method uses a computational expensive iteration technique for each time step but in return quite large time steps can be applied. It is also possible to solve a problem in one time step. For highly non-linear problems this method may lead to difficulties. In case of e.g. quickly changing stiffness the solver will need many iterations to obtain a result. This can lead to extended computing time or the solver may not be able to find a solution. Examples might be material failure or a changing contact condition. Such a scenario is visualized in figure 2.11. For such a problem a higher number of time steps is necessary to reduce the iteration effort. Alternatively the explicit solver can be utilized. The explicit methods works with the following equation 2.14 for time t_{n+1}:

$$k \cdot u_{n+1} = F_{n+1} \tag{2.14}$$

As visible in the equation the explicit technique simply uses the stiffness matrix of the previous time step to compute the displacement for each time step. The iteration of the force equilibrium is

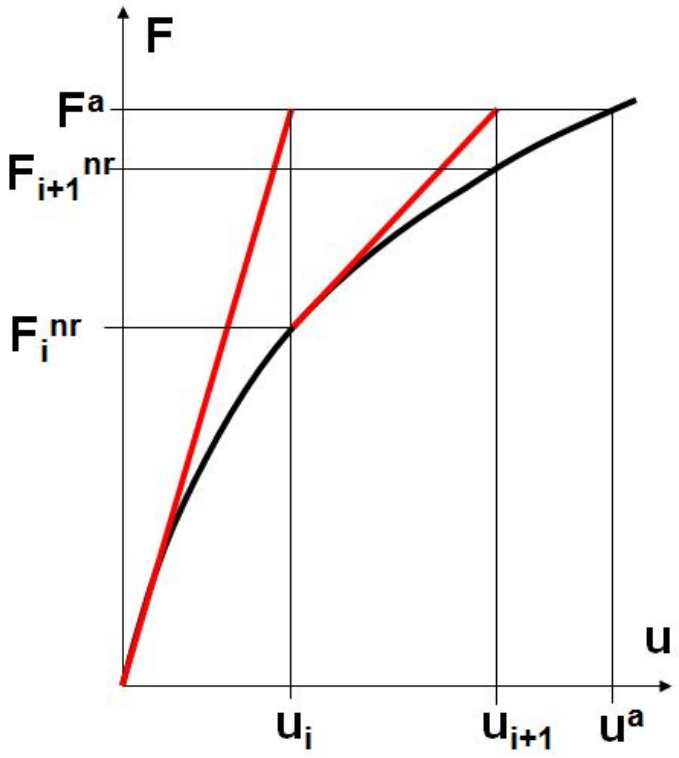

Figure 2.10: The Newton-Raphson method(CAE-Wiki, 2015).

not necessary here. Hence the computation of one time step is very fast. On the other side the time steps need to be quite short. In case of a large time step using the stiffness matrix of the previous time step is inaccurate. This is especially important because the maximum step time is dependent on the length l of the smallest edge of all elements.

$$\delta t_{max} = \frac{l}{c_s} \tag{2.15}$$

The reason is that a shockwave which travels with the speed of sound will skip an element if the time step is larger. So the mesh has a significant influence on the computation time. The main advantages of the explicit solver are its robustness in case of highly non-linear problems and its capability to consider dynamic effects. Due to that the explicit solver of LS-Dyna will be used to analyse dynamic loads on the GoSolAr such as a docking scenario. The implicit method is preferable in case of long transient dynamics or static problems. Due to the iterative method the solver will provide the best results for static load cases such as the atmospheric drag or solar radiation pressure. However the implicit solver is inapplicable for short dynamic load cases such as docking. (Gebhardt, 2014)

2.4 Study of the current design

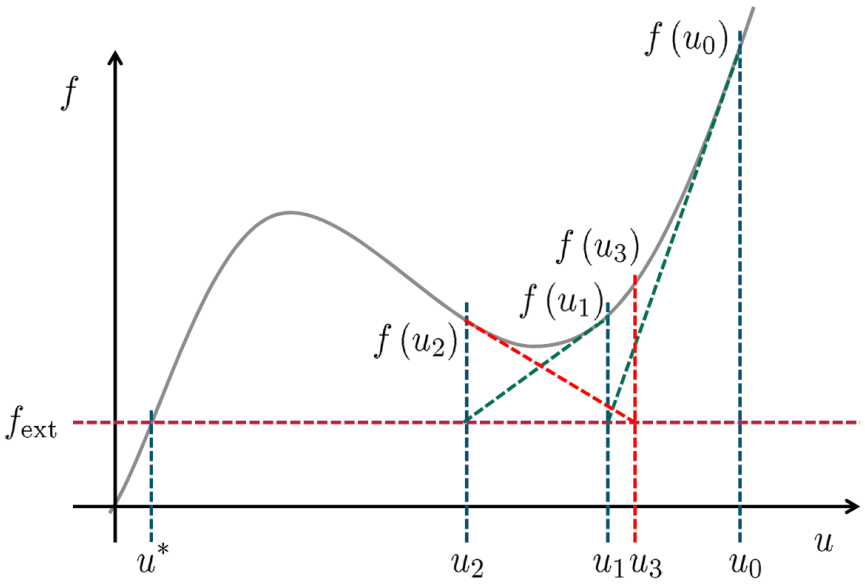

Figure 2.11: Non converging Newton Raphson method(Bl and Bolea Albero, 2016).

3 The finite element analysis (FEA)

In the following the finite element analysis which is performed on the GoSolAr is described in more detail. The analysis consists of a modal analysis, a static analysis and a dynamic analysis. It will be shown how the geometrical model is built as well as the approach for the following analyses. The FEA is performed with the software Ansys workbench. The simplified model of the solar array is built with the help of Catia V5 and Ansys DesignModeler.(**?**)

3.1 Creating the model

3.1.1 The geometry

As mentioned before the geometry of the GoSolAr is transformed to a simple model consisting of beam and shell elements in order to do the FEA with small computing effort. The photovoltaic cells, the membrane and the harness will be modelled using shell elements and the masts are represented by simple beams. For the FEA two different geometric models are made. A quarter model is made to analyse simple symmetric static and dynamic load cases to reduce the computing effort. For asymmetric load cases and the modal analysis a full model of the solar array is needed. The full model of the solar array is visualized in figure 3.1. It consists of quadratic shell elements that

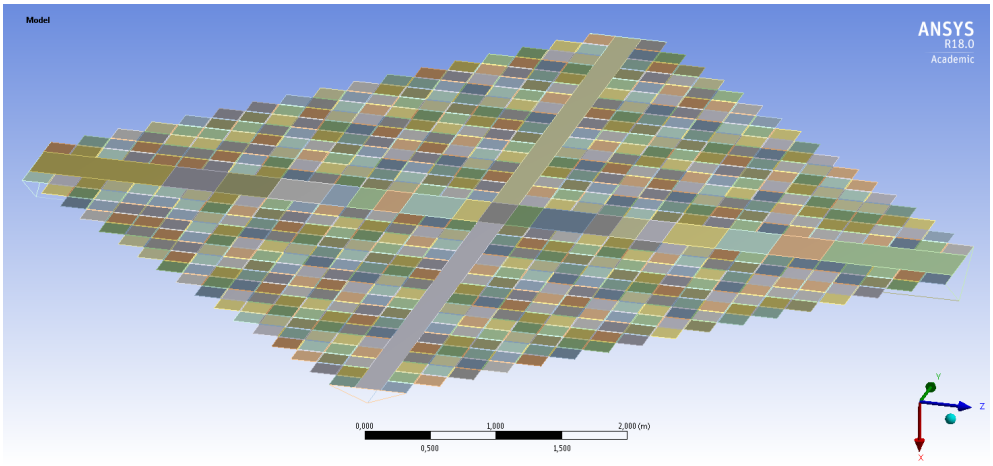

Figure 3.1: The full model of the array.

represent the photovoltaic cells. All cells are connected by narrow shell elements representing the membrane between the cells and the string harness which connect the PV elements to each other (figure 3.2). The area which represents the main harness is separated into 9 parts, each with another thickness representing the multiple main harness layers. The middle gap consisting of membrane

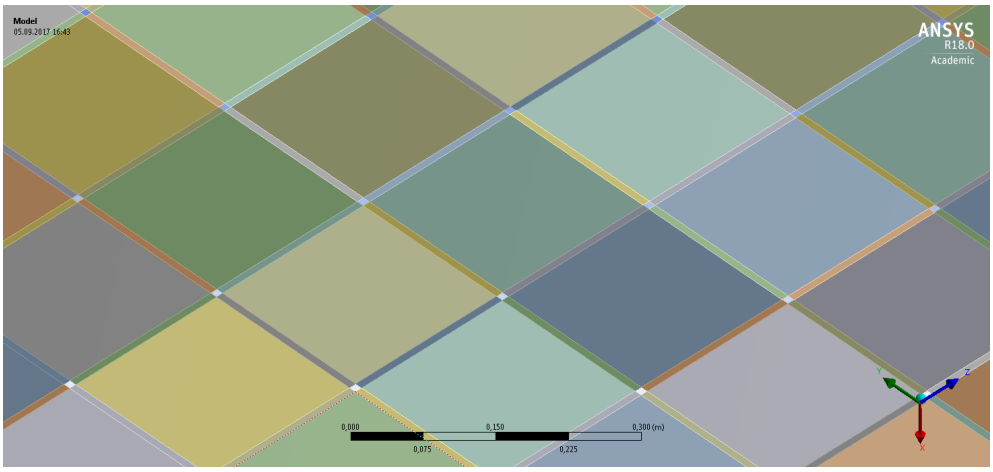

Figure 3.2: Detail view of the connections.

foil between the photovoltaic cells is modelled by one long shell element. The masts are modelled by line bodies. The cross section of the mast is simulated by applying the second moments of inertia and the cross sectional area of applicable masts that are provided by the DLR Institute of Composite Structures and Adaptive Systems. The properties of the applicable masts are stated in table 3.1. The quarter model is created by sectioning the full model and removing 3 quarters of the model. Additionally the properties of the masts are modified. The second moment of inertia about the horizontal axis is halved. The second moment of inertia about the vertical axis is irrelevant in this case because the symmetry constrain blocks rotation and movement in the corresponding directions. The cross sectional area is also halved. The quarter model is visualized in figure 3.3.

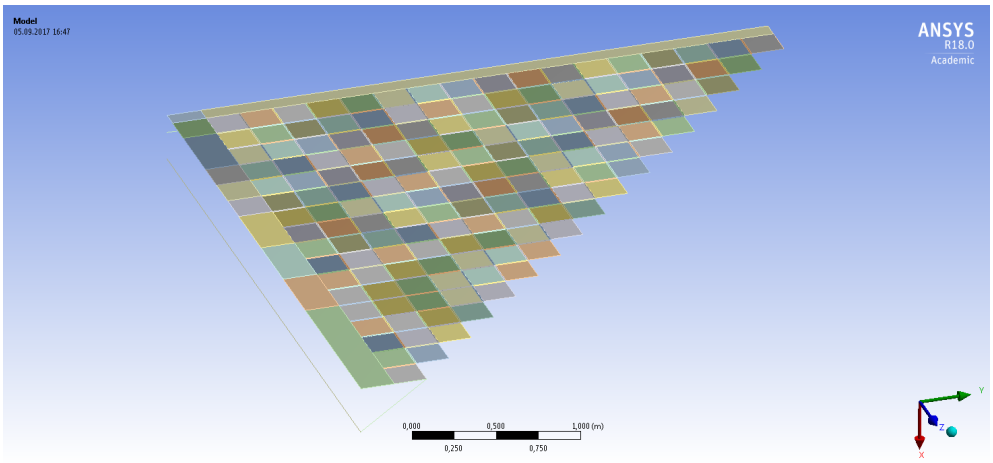

Figure 3.3: The quarter model of the array.

3.1.2 The materials

Simple materials are created in Ansys and allocated to each element. Only the Young's modulus and the density are applied. The poisson's ratio is set to a default value of 0.3. For the multilayer

Mast type	Young's modulus in $\frac{N}{mm^2}$	Density in $\frac{kg}{m^3}$	I_{xx}	I_{yy}	Corss sectional area in m^2
Goss 2	$6 \cdot 10^{10}$	1600	$8.555 \cdot 10^{-8}$	$8.632 \cdot 10^{-8}$	$23.75mm^2$
Goss 1	$6 \cdot 10^{10}$	1600	$5.742 \cdot 10^{-9}$	$7.515 \cdot 10^{-9}$	$40mm^2$
DeOs	$6 \cdot 10^{10}$	1600	$1.489 \cdot 10^{-9}$	$2.288 \cdot 10^{-9}$	$127.5mm^2$

Table 3.1: Material properties of the masts.

components such as the PV cells the Young's modulus and the density were averaged. The averaging of the Young's modulus is done using the formula:

$$Y_{total} = \frac{\sum_0^n Y_n \cdot h_n}{h_{total}} \tag{3.1}$$

where Y_n is the Young's modulus and h_n is the thickness of each layer. The density is averaged in the same manner:

$$\rho_{total} = \frac{\sum_0^n \rho_n \cdot h_n}{h_{total}} \tag{3.2}$$

This approach is applied determining the material properties of the PV cells and of the harness. In terms of the string harness it has to be considered that the string harness is not 200 mm wide but only 160 mm. To consider this the harness is modelled with a width of 200 mm and the stiffness is reduced to compensate that. In this case a substitute stiffness of 80 % of the harnesses stiffness is used for the corresponding elements that connect the PV elements. By this approach a change of the width of the harness can be easily considered without modifying the geometry. Furthermore this needs to be considered when the average properties of the PV cells are determined. Hence the thicknesses of the layers of the harness are multiplied with 0.8. table 3.2 and table 3.2 show the material properties of the component materials, their thicknesses and the averaged properties. The

PV generator	Thickness in µm	Young's modulus in $\frac{N}{mm^2}$	Density in $\frac{kg}{m^3}$
Copper indium gallium selenide (CIGS)	5	7100	5700
Polyimide	25	9120	1470
Adhesive	75		
Polyimide	25	9120	1470
Copper	35	115000	8920
Polyimide	25	9120	1470
Adhesive	75		
Polyimide	$25 \cdot 0.8$	9120	1470
Copper	$35 \cdot 0.8$	115000	8920
Ag	$0.1 \cdot 0.8$	80000	10500
SiO_2	$2 \cdot 0.8$	76500	2650
Composite	327.1	27300	2336

Table 3.2: Material properties of the layers of the PV generator.

material properties for the adhesive are not available. The density and the Young's modulus are very low compared to the other materials and therefore assumed to be zero in the calculation. Due to the very small density and Young's modulus this assumption only leads to a very small error in the composite properties which is negligible.

Harness	**Thickness in µm**	**Young's modulus in $\frac{N}{mm^2}$**	**Density in $\frac{kg}{m^3}$**
Polyimide	25	9120	1470
Copper	35	115000	8920
Ag	0.1	80000	10500
SiO_2	2	76500	2650
Composite	62.1	71079	5721

Table 3.3: Material properties of the layers of the harness.

3.2 Modal analysis

Due to the low stiffness of the GoSolAr the natural oscillation is a major critical point. It is important to have knowledge about the natural frequencies of the array with special respect to the positioning control of a S/C. The positioning control should avoid the low eigenfrequencies of the array. A very low natural frequency is expected due to the low stiffness. It is desired to attain an eigenfequency as high as possible while having small modal masses. The natural frequency of the array is highly dependent on the pre stress of the PV sail. When the sail will be deployed the masts will put a specific force in the PV sail to tension it. Considering that generally a tensional stress causes an increase of stiffness and a compressive stress causes a decrease of stiffness and looking at the problem solely by using the simple formula for the eigenfrequency

$$\omega = \sqrt{\frac{k}{m}} \tag{3.3}$$

leads to the assumption that putting a tensile pre stress on the PV surface increases the natural frequency and on the other hand the natural frequency of the masts decreases when they are under compression pre stress. Hence the correlation between the pre stress and the eigenfrequency is not necessarily a monotonic one because both effects may be present. Banik (2014) states in his work that in such a case the natural frequency will increase with increasing pre stress up to a certain point. From this point onwards the frequency decreases again. It is possible that a similar behaviour of the eigenfrequency of the GoSolAr appears. Thus the behaviour of the PV array is examined and the highest possible eigenfrequency is to be determined. In the following the dependencies of the eigenfrequencies and the modal masses from the pre stress on the array are evaluated to gain knowledge on how much pre stress is to be applied. Additionally it is evaluated how the different masts influence the behaviour of those values. Thus the modal analysis is done with different pre stresses and different masts.

3.2.1 Analysis settings

To simulate the pre stress in the masts they are pushed outwards by forces. Due to that the masts are seperated in the centre. As shown in figure 3.4 four forces will be applied at the centre, one on

each mast. The vertex on which the force is applied is constrained so it can only move in the force's direction. Movement in any other direction or rotation is prohibited. The centre of the array is fixed with a fixed support simulating the inferface. When pushing the masts outwards the masts are under compression stress and the sail is under tensile stress. The pre stress simulation is done with large deflections "on" so the implicit solver is used. The force is increased over several time steps which are evaluated in the modal analysis. In the low force region the time steps are very small. The δF is between 0.2 and 0.4 N. This is due to the fact that a very small pre tensioning force is assumed to be used on the final array. So this region is examined with a higher resolution. Nevertheless higher forces are also examined. From 3 N on the time steps are larger with a δF between 2 and 4 N to reduce the analysis effort. Generally a higher force can be applid on the stiffer masts. This is due to the fact that the less stiff masts cause larger deflections than the stiffer masts applying the same force. When the deflections beome very large the solver is not able to find a solution anymore. Thus a maximum force of 24 N is applied to the Gossamer-2 mast. The Gossamer-1 and the DeOs mast are evaluated with forces up to 10 N and 3 N respectively.

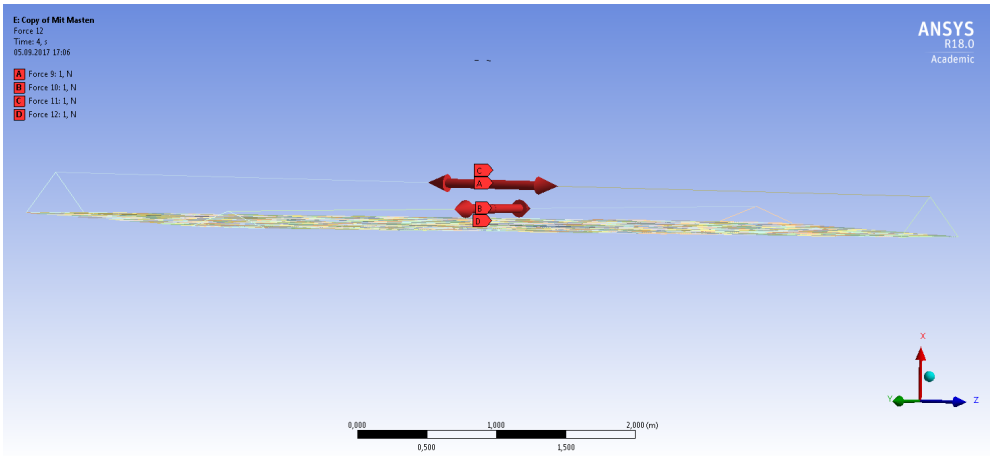

Figure 3.4: The forces that simulate the pre stress on the masts.

3.2.2 Mesh convergence study

In order to prevent poor results from an insufficient mesh density, a mesh convergence study is carried out. It is done on the photovoltaic array equipped with the Gossamer 2 mast. A force of 22 N is applied on each mast and the natural frequency is evaluated for several different mesh resolutions. Therefor the mesh relevance is changed in a range between -100 and 60. The lowest eigenfrequency is determined and plotted against the mesh relevance. Figure X shows the results. The results show that there is no significant dependency of the natural frequency on the resolution of the mesh. The difference between the lowest and the highest natural frequency is 0.107 % which is negligible. Hence the simulations can be done with a coarse mesh. No matter how fine the mesh relevance is set the connecting elements which represent the harness and the membrane foil never have more than one element perpendicular to the longitudinal axis (fig X). To rule out that this may have an impact on the results a mesh refinement was done on these elements (fig X). The difference between the results with and without mesh refinement is 0.695 %. The difference is relatively small considering the excessive increase in computing effort due to the mesh refinement and therefore

neglected. Due to the fact that changes in the mesh have no significant impact in any case a very coarse mesh is selected for the analysis selecting a mesh relevance of -100 with no mesh refinements for the Gossamer-2 mast. In case of the less stiff masts a denser mesh was required due to the larger deflections. With the very coarse mesh the solver was not able to come to a solution because the deflections are much larger due to the more flexible masts. Hence, the mesh relevance was set to 0 in case of the Gossamer-1 mast and to 40 for the DeOs mast. These values result in elements sizes of 33.33 mm (Gossamer-2), 16,67 mm (Gossamer-1) and 12.5 mm (DeOs) respectivley according to the mesh of the PV generators.

3.2.3 Buckling load

To set a limit of the applicable pre tensioning force on the masts, the buckling loads are calulated. A maximum allowable buckling load of one third of the theoretical Euler buckling load must not be exceeded. The load case for that is visualized in figure 3.5 is assumed for the calculation. The buckling load of the corresonding load case is calculated as follows:

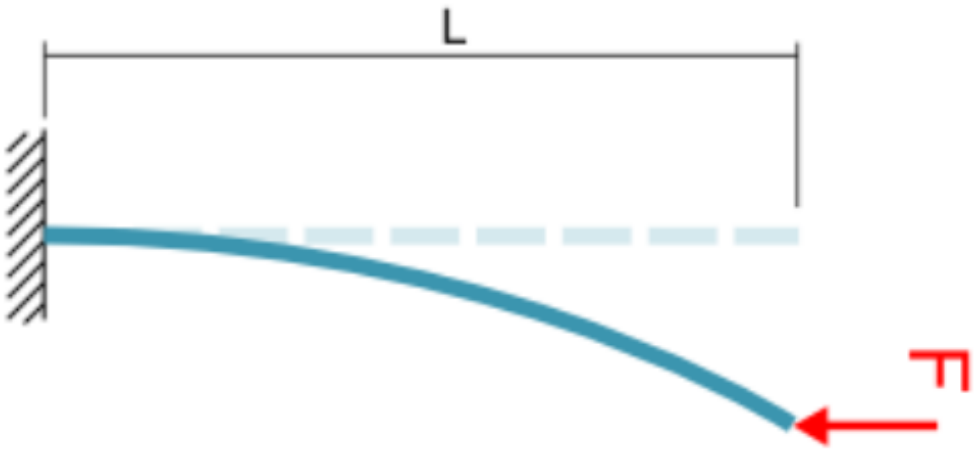

Figure 3.5: The buckling load case.

$$F_{crit} = \frac{\pi^2}{4 \cdot l^2} \tag{3.4}$$

So for the Gossamer 2 mast the maximum load is:

$$F_{crit,Gos2} = 900.83N \tag{3.5}$$

$$\frac{F_{crit,Gos2}}{3} = 300.28N \tag{3.6}$$

The buckling loads for the Gossamer 1 and DeOs mast are:

$$F_{crit,Gos1} = 60.46N \tag{3.7}$$

$$\frac{F_{crit,Gos1}}{3} = 20.15N \tag{3.8}$$

$$F_{crit,DeOs} = 15.68N \tag{3.9}$$

$$\frac{F_{crit,DeOs}}{3} = 5.23N \tag{3.10}$$

All of the assumed critical buckling loads are higher than the analyzed range. Hence, the buckling load is not a considerable influence quantity.

3.3 Results of the modal analysis

In the following the results for each mast are presented.

3.3.1 Gossamer 2 mast

The Gossamer 2 mast is the stiffest and heaviest one. Its weight is 3.01712 kg for all 4 masts. The first 10 natural frequencies are plotted against the pre-stress in figure 3.6. As visible in the graph

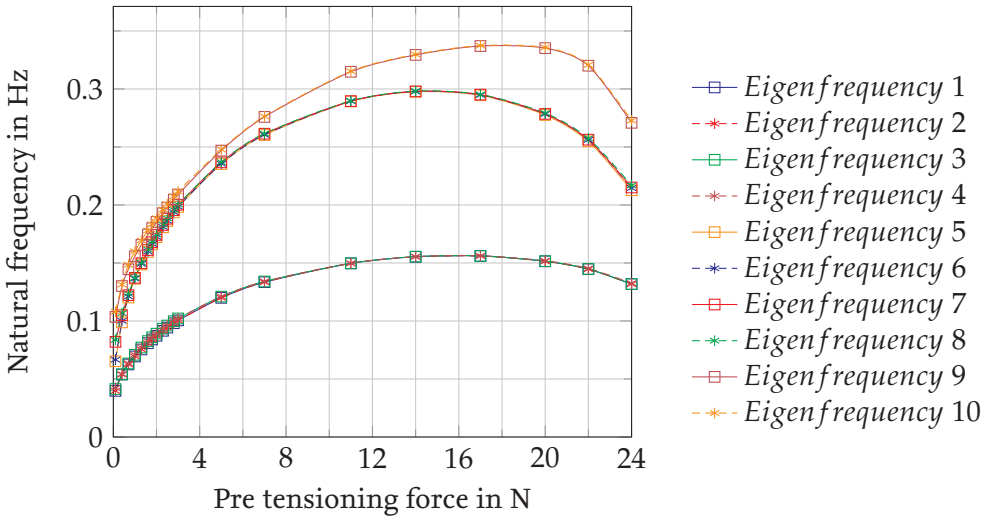

Figure 3.6: The first 10 eigenfrequencies of the array with the Gossamer 2 mast.

the natural frequencies 1 to 4, 5 to 8 and 9 and 10 are very similar. This is due to the symmetry of the array. As visible in figure 3.7 the shapes of the modes 1 to 4 are basically the same but only the directions of the antinodes are different. Thus it can be assumed that the similar frequencies are representing the same natural frequency. The occurring mode shape is assumed to be dependent on the excitation which the array undergoes. Therefore when speaking about the first natural frequency group the natural frequencies 1 to 4 are meant. The same applies to the natural frequencies 5 to 8. It is not unlikely that the third eigenfrequency has more than the two calculated mode shapes. Because of that the third eigenfrequency is not evaluated. The modal masses are also influenced by the pre tensioning force. The modal masses of the mode shapes of each eigenfrequency are added up and plotted against the pre tensioning force. Only the modal masses in the X-direction and the rotation masses about the Y- and Z-axis are considered. In the other directions there are no significant modal masses. The following figures show the graphs for the modal masses against the pre tensioning force.

X direction

For the modal mass of the first eigenfrequency in the X-direction the first mode shape shown in figure 3.7 is responsible. In this mode shape all quadrants swing uniformly. The second eigenfrequency has no modal mass in X-direction. The antinodes always are always neutralizing each other as visible in figure 3.8. They never swing uniformly. The modal mass of the first natural frequency decreases with increasing pre stress. So in terms of the modal mass in the X-direction a high pre

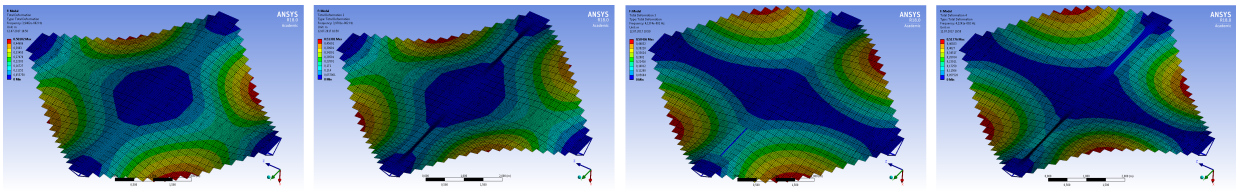

Figure 3.7: The mode shapes of the first eigenfrequency group for a pre tensioning force of X N on the Gossamer-2 mast.

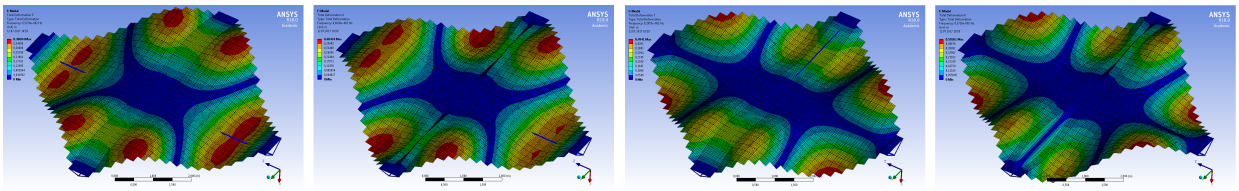

Figure 3.8: The mode shapes of the second eigenfrequency group for a pre tensioning force of X N on the Gossamer-2 mast.

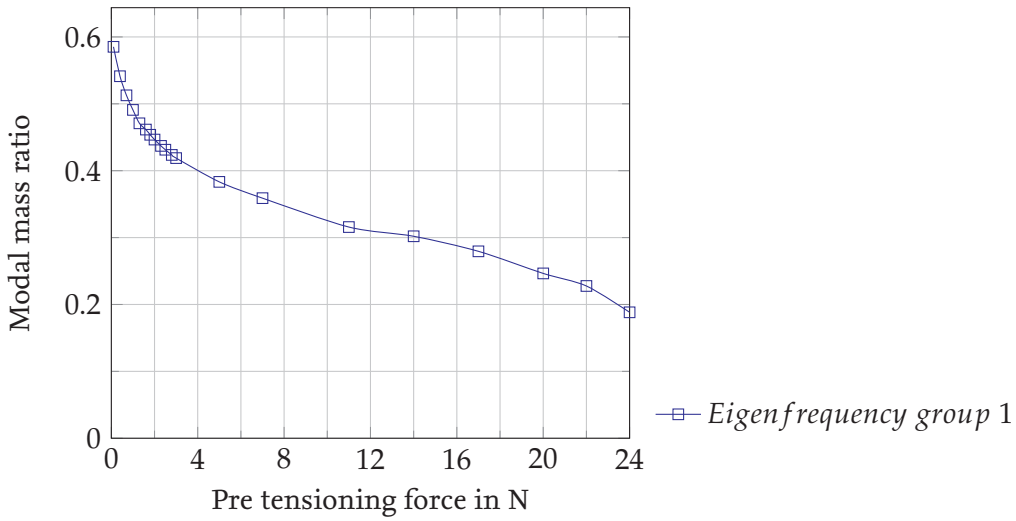

Figure 3.9: The modal masses in X direction (Gos-2).

stress is desirable.

Y rotation

For the rotation mass of the first eigenfrequency second mode in figure 3.7 is responsible. Regarding the second eigenfrequency the second mode shape shown in figure 3.8 is responsible. In the graph it can be seen that the modal mass of the first eigenfrequency decreases with increasing preload force. The modal mass of the second eigenfrequency has a small peak when very low force is applied. It decreases with increasing pre stress until about 3 N and then increases slightly. Higher pre tensioning again causes a decrease in the modal mass. In terms of the rotational modal mass around the Y-axis the load should be as high as possible.

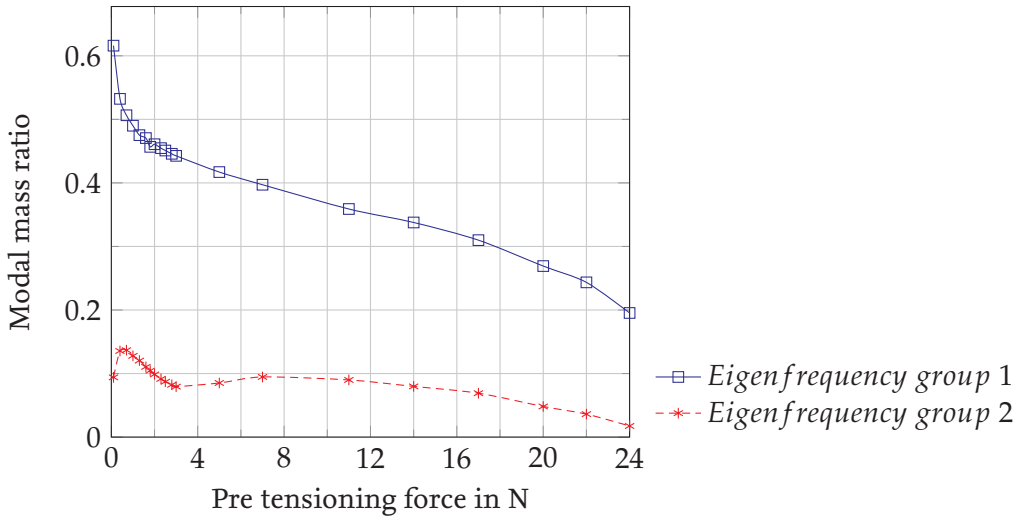

Figure 3.10: The rotational modal masses about the Y axis (Gos-2).

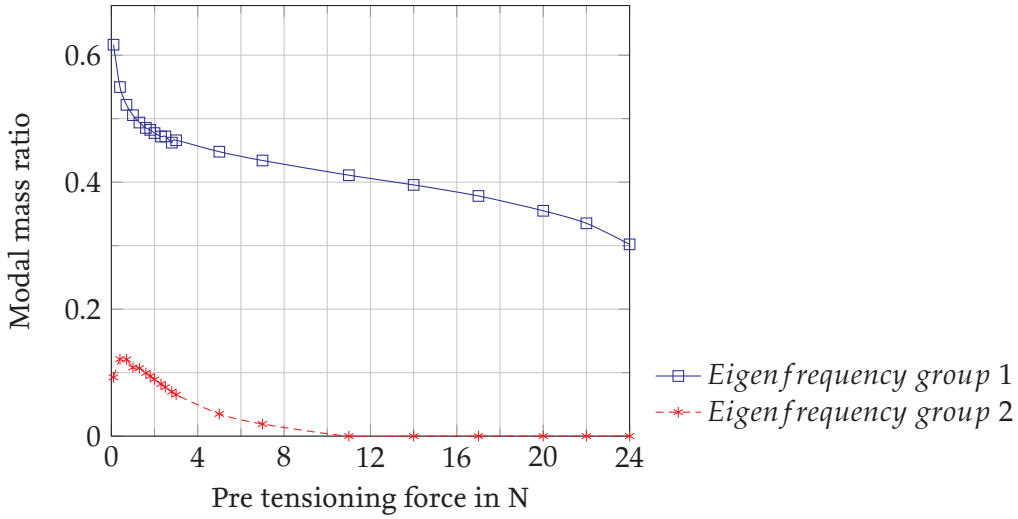

Figure 3.11: The rotational modal masses about the Z axis (Gos-2).

Z rotation

figure 3.11 shows the dependence of the rotational modal mass about the Z-axis on the preload force. The thrid mode shape in figure 3.7 is responsible for the rotational mass about Z for the first eigenfrequency. The rotational mass about Z in the second natural frequency is due to the third mode shape in figure 3.8. The modal mass of the first eigenfrequency decreases with increasing pre stress. The modal mass of the second natural frequency has a peak when very low preload force is applied and then decreases with increasing force until it is zero from around 11 N on. In terms of the rotational mass about Z the preload force of 17 N is also the optimal force in terms of modal masses.

Recommondation

As visible in figure 3.6 the optimal pre tensioning force is between 14 N and 17 N considering the first natural frequency. With regard to the modal masses a force of 17 N is more advisable. The optimal pre tensioning force of 17 N is not critical in terms of modal masses. In the order of magnitude of the optimal pre tensioning force lowering the force will lower the eigenfrequencies and increase the modal masses, which is both undesirable. Increasing the force to further than 17 N will always lower the modal masses but at the same time decrease the eigenfrequencies. It may be advisable to increase the preload force to a level where there is no significant decrease in the eigenfrequency but a significant decrease in modal masses. For example increasing the preload force from 17 N to 20 N leads to a decrease of the first natural frequency from 0.156 Hz to 0.152 Hz, which is 2.9 %. At the same time the modal masses in X direction and the rotational masses about Y and Z of the first eigenfrequency decrease by 11.8 %, 13.2 % and 6.2 % respectively. The rotational mass about Y of the second eigenfrequency decreases by 30.3 % while decreasing the second eigenfrequency by 5.6 %. This shows that it may be worth accepting slightly lower natural frequencies to lower the modal masses significantly.

3.3.2 Gossamer 1 mast

The Gossamer 1 mast is lighter and less stiff than the Gossamer 2 mast. The 4 masts weigh 0.94652 kg. In figure 3.12 the eigenfrequencies of the array with the Gossamer 1 mast is plotted against the pre tensioning force. Compared with the array with the Gossamer 2 mast the eigenfrequencies

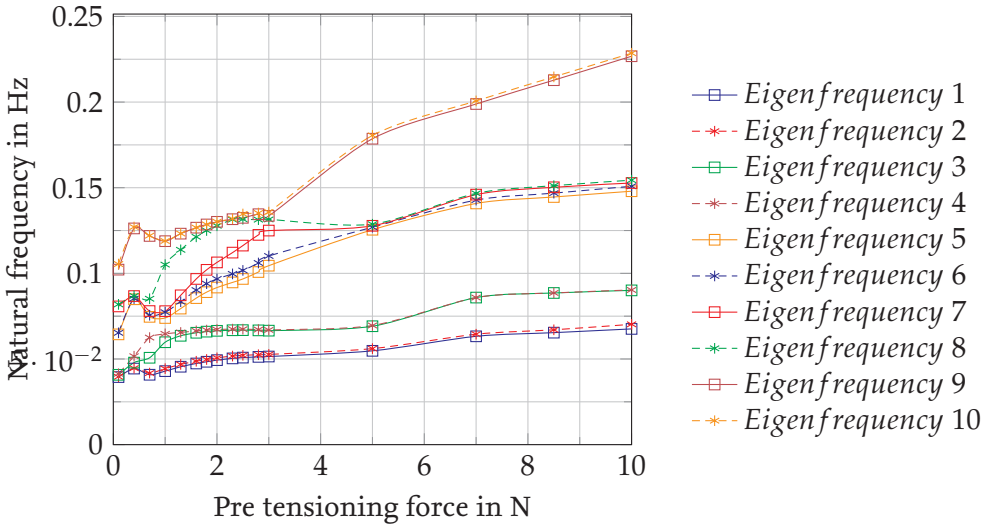

Figure 3.12: The first 10 eigenfrequencies of the array with the Gossamer 1 mast.

behave more uneven especially when low force is applied on the masts. When higher pre stress is applied it becomes clear that there are 4 eigenfrequencies, each with at least two mode shapes but the number of mode shapes for each major eigenfrequency changes with lower pre stress. So the eigenfrequencies are not grouped in major eigenfrequencies but grouped by similar mode shapes. As before two groups will be evaluated in more detail. The first group is the one with one antinode per quadrant. The second group has 2 antinodes per quadrant. The mode shapes of the groups are exemplary visualized for a pre tensioning force of 1.3 N in figure 3.13 and figure 3.14.

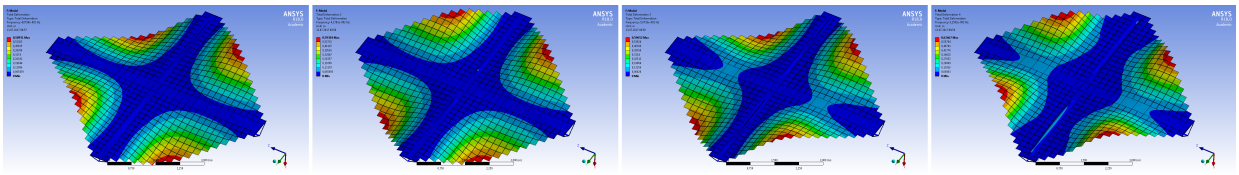

Figure 3.13: The mode shapes of the first eigenfrequency group for a pre tensioning force of 1 N on the Gossamer-1 mast.

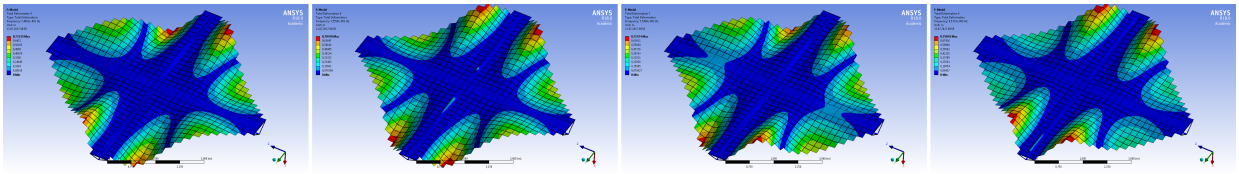

Figure 3.14: The mode shapes of the second eigenfrequency group for a pre tensioning force of 1 N on the Gossamer-1 mast.

X direction

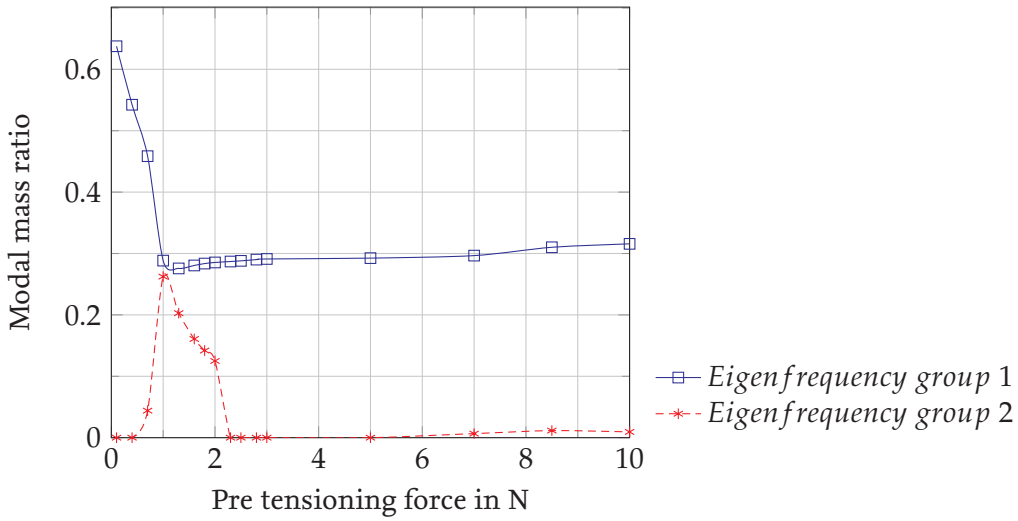

Figure 3.15: The modal masses in X direction (Gos-1).

Both mode shape groups have modal masses in X-direction. The fourth mode shape in figure 3.13 is responsible for the modal mass in X direction. All quadrants swing uniformly. The modal mass of this natural frequency is very high when low pre tensioning force is applied. An increase in the force leads to a decrease of the modal mass. A minimum is reached at around 1 N. Increasing the force any further causes a slight increase of the modal mass. The other modal mass in X direction is due to the fourth mode shape in figure 3.14. There is a peak in the modal mass at 1 N. Further increase of the pre stress lowers the modal mass until it is zero at about 2.3 N. There is another slight increase at high pre tensioning force.

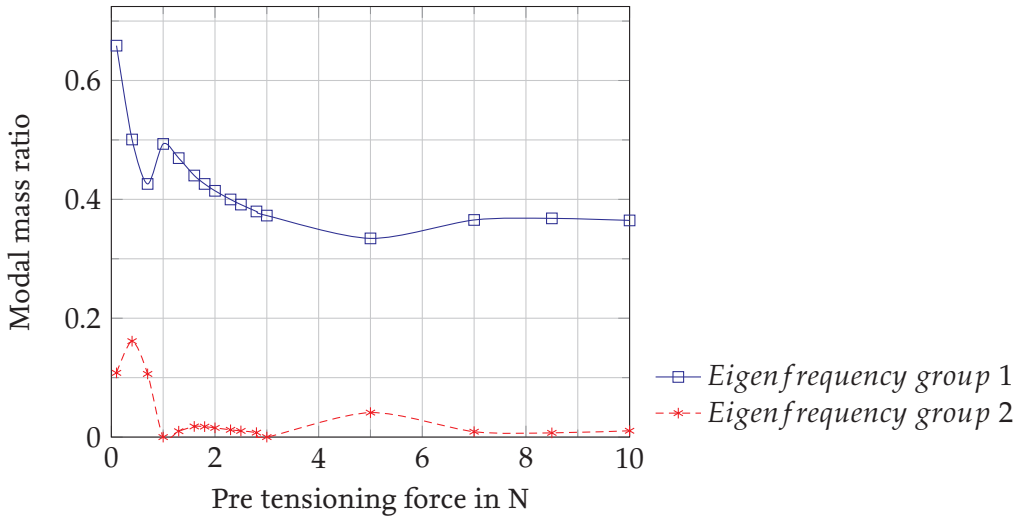

Figure 3.16: The rotational modal masses about the Y axis (Gos-1).

Y rotation

In terms of the rotational mass about the Y-axis the third mode shape in figure 3.13 and the third mode shape in figure 3.14 are responsible. The modal mass of the lower natural frequency decreases with higher pre tensioning force until about 5 N. From there on the modal mass slightly increases and then remains constant. The modal mass of the higher natural frequency also decreases with increasing force. From 1 N on it remains nearly zero except of a small peak at 5 N. Regarding the rotational mass about the Y-axis a preload force as high as possible is desirable.

Z rotation

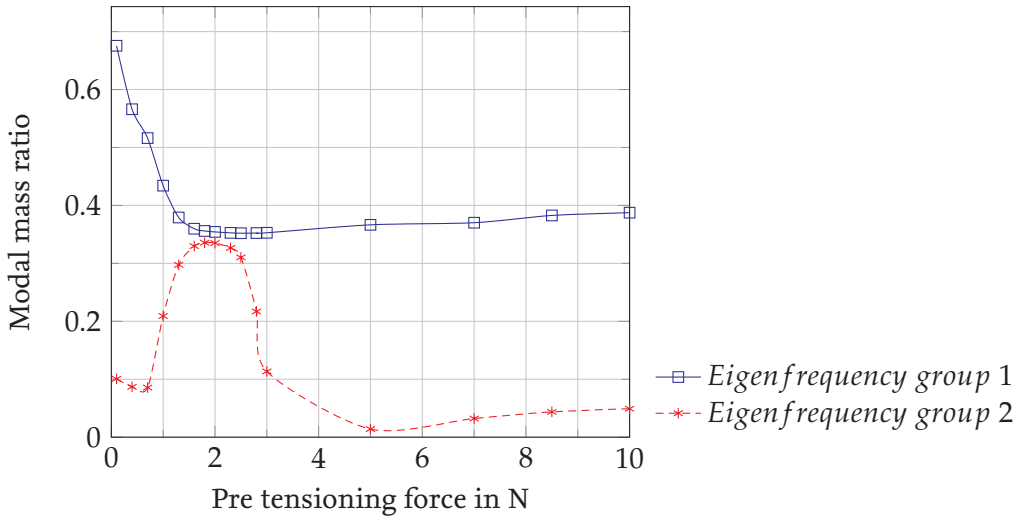

Figure 3.17: The rotational modal masses about the Z axis (Gos-1).

The modal rotational mass about the Z-axis is due to the second mode shape in figure 3.13 and the second mode shape in figure 3.14. The modal mass of the lower eigenfrequency decreases with

increasing preload force until about 2 N and then slightly increases again. The modal mass of the higher eigenfrequency has a peak around 2 N and then decrases with increasing force until around 5 N. Then it increases slightly with increasing force. In terms of the Z rotational mass low preload forces are to be avoided. A preload force of around 5 N is advisable. Lower pre stress should be avoided due to a significant increase of the modal mass. Higher pre stress only slightly increases the modal mass.

Recommondation

In terms of the natural frequency a pre tensioning force s high as possible is dersirable. Genereally the modal mass decreases with increasing pre stress. But in the low stress region e.g the rotational mass about the Z axis and the mass in X direction for the higher eigenfrequencies have a peak. Hence, a pre tensioning force of at least about 3N is advisble because all peaks in the modal mass are overcome. A higher pre tensioning force does not significantly lower the modal masses anymore. Hence, the pre tensioning force should be as high as possible but should at least be more than 3 N.

3.3.3 DeOs mast

The DeOs mast is the lightest mast. All four masts together have a weight of 0.56202 kg. The natural frequency of the array equipped with the DeOs mast increases with increasing pre tensioning force. The behaviour of the eigenfrequencies is much more complex than for example the ones of the array with the Gossamer 2 mast. The plot is shown in figure 3.18. As before they are grouped regarding their mode shapes. For example the mode shapes of the eigenfrequencies 1 to 4 are very similar as figure 3.19 shows. Each quadrant has only one antinode. The second basic mode shape is the one with two antinodes per quadrant which is given in figure 3.20.

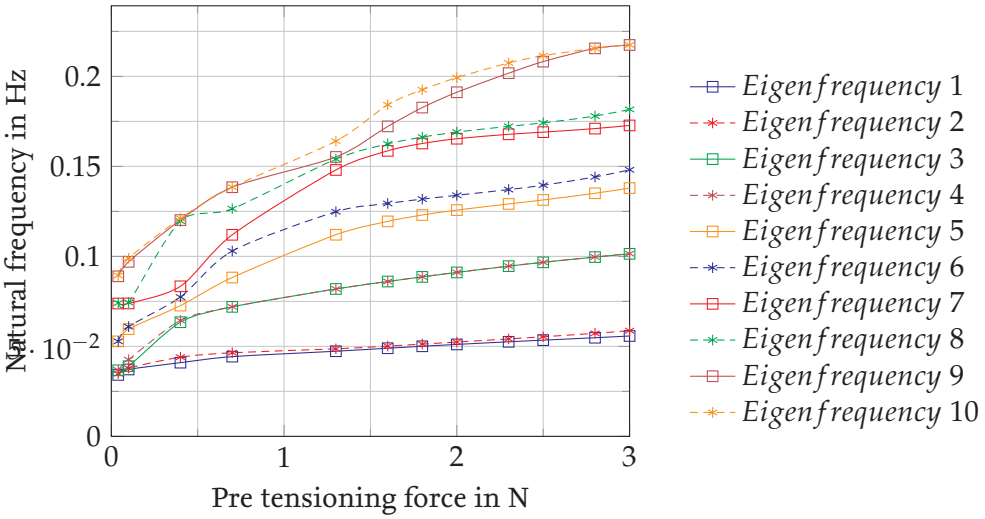

Figure 3.18: The first 10 eigenfrequencies of the array with the DeOs mast.

X dircetion

The modal mass in the X-direction of the lower eigenfrequencies decreases with increasing pre stress. Above 2 N a minimum is reached and the modal mass remains constant. The modal mass is due to the fourth mode shape in figure 3.19 where all quadrants swing in the same direction. The

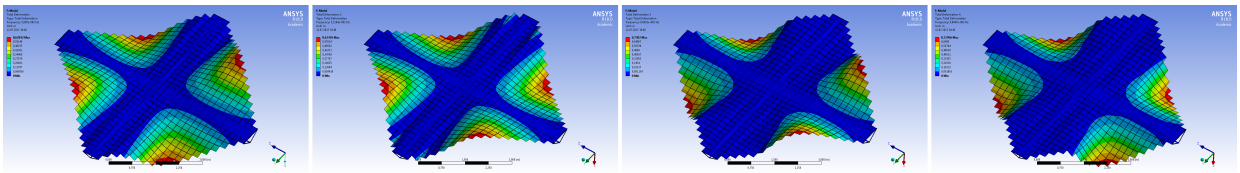

Figure 3.19: The mode shapes of the first eigenfrequency group for a pre tensioning force of X N on the DeOs mast.

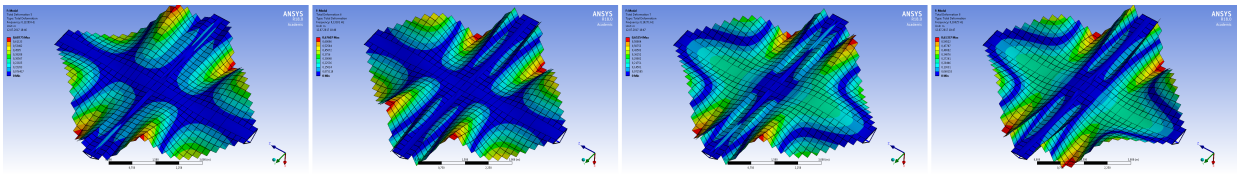

Figure 3.20: The mode shapes of the second eigenfrequency group for a pre tensioning force of X N on the DeOs mast.

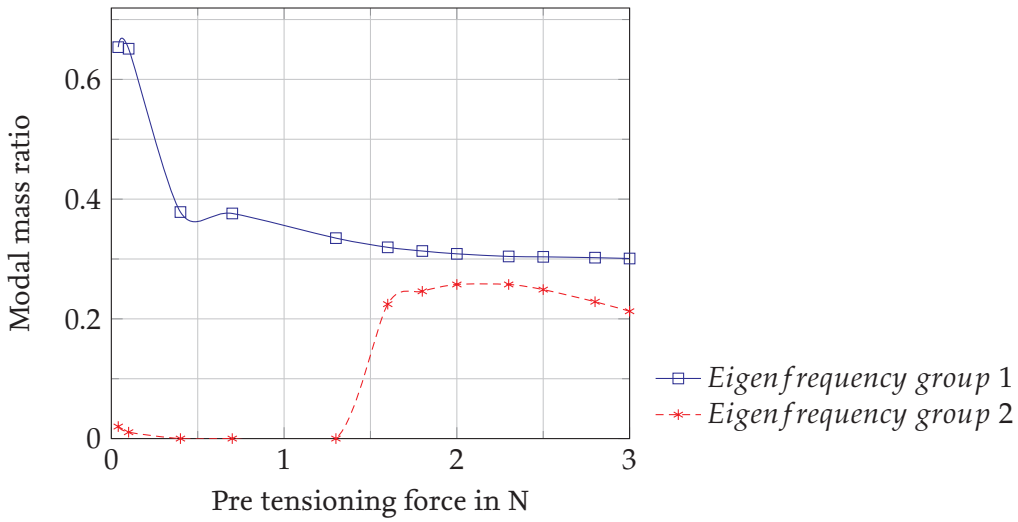

Figure 3.21: The modal masses in X direction (DeOs).

modal mass of the higher eigenfrequencies is zero at low pre stress. Around 1.5 N the modal mass increases abruptly and slightly decreases again when the preload force exceeds 2 N. So in terms of the modal masses in X direction a pre tensioning force between 0.5 N and 1.5 N is advisable. The modal mass of the higher eigenfrequencies in X direction is caused by the fourth mode shape in figure 3.20.

Y rotation

The rotational mass about the Y axis of the lower eigenfrequency basically decreases with increasing pre stress. The modal mass of the higher eigenfrequeny has a small peak at a pre stress of 0.1 N. At 0.4 N the modal mass is zero and then increases until about 1.8 N. Higher forces again decrease the modal mass. Here a pre stress as high as possible is desirable. The corresponding mode shapes are the one in figure figure 3.19 and the third one in figure 3.20.

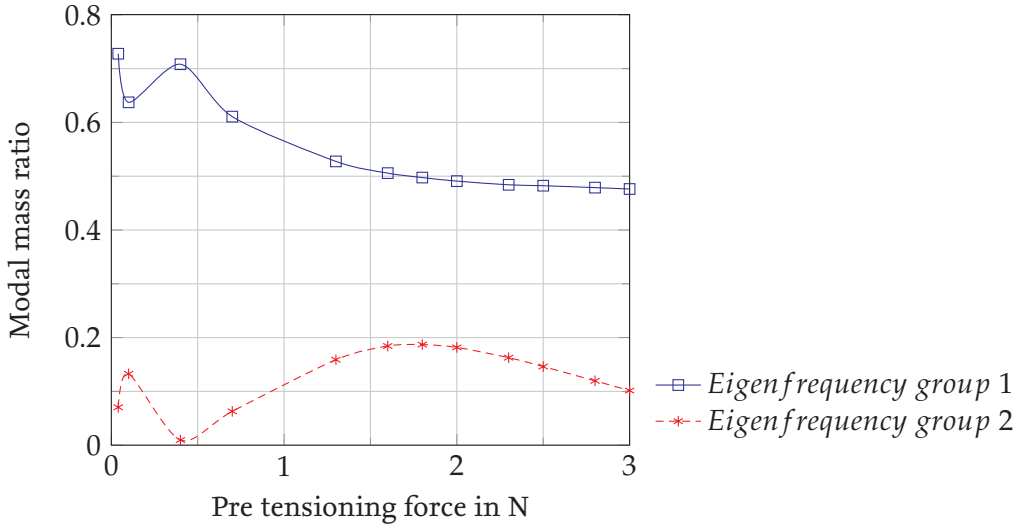

Figure 3.22: The rotational modal masses about the Y axis (DeOs).

Z rotation

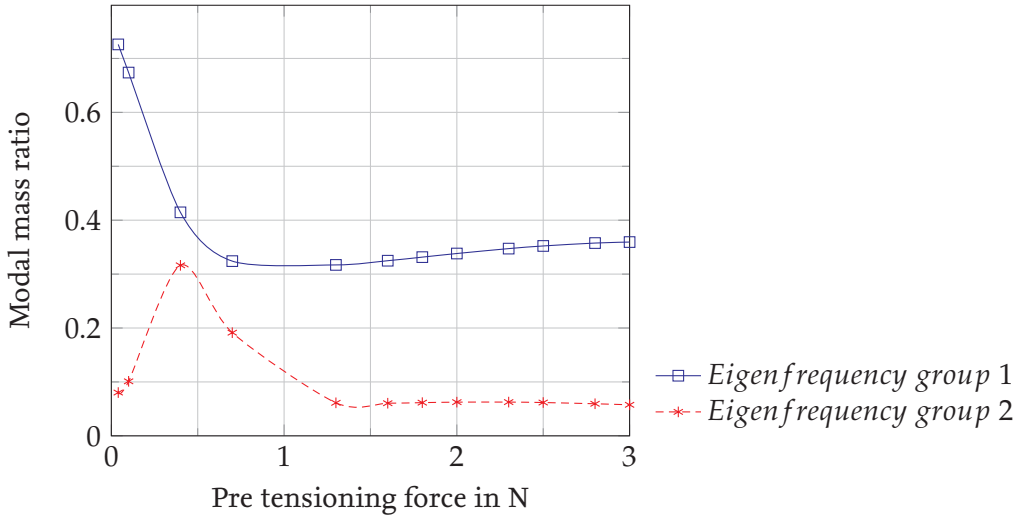

Figure 3.23: The rotational modal masses about the Z axis (DeOs).

In terms of the rotational masses about the Z axis the modal mass of the lower eigenfrequency decrases with increasing pre stress until about 1 N and then slightly increases again. The mode shape is the second one in figure 3.19. The modal mass of the higher eigenfrequency has a peak at about 0.5 N and then decreases with increasing pre stress. The corresponding mode shape is the second one in figure 3.20. Regarding the rotational masses about the Z axis a pre stress of about 1.5 N is optimal but higher pre stress does not significantly increase the modal masses.

Recommondation

Regarding the eigenfrequencies the pre tensioning force should be as high as possible. But it has to be mentioned that an increase of the pre tensioning force does not significantly increase the

first eigenfrequency. The modal masses of the lower eigenfrequency do not significantly decrase anymore when force of more than 1 N is applied. The modal mass in X direction and the rotational mass about the Y direction even increase when a higher pre tensioning force than 1 N is applied. Thus a pre tensioning force of about 1 N is advisable. Higer force does not significantly increase the eigenfrequency but even increases the modal masses of the higher eigenfrequency.

3.3.4 Evaluation of the results of the modal analysis

In order to compare the three masts better only the range between 0 and 3 N and only the first natural frequencies are considered. The first natural frequency of the Gossamer 1 and the DeOs mast are nearly the same. The one of the DeOs mast is slightly higher. The eigenfrequency of the Gossamer 2 mast is much higher. When applying a pre tensioning force of 3 N it is about twice as high as the eigenfrequency of the other masts. To explain this behaviour the results of the static pre tensioning need to be evaluated. In the folowing the Gossamer 2 mast and the DeOs mast are opposed. figure 3.24 and figure 3.25 show the normal stresses of the two masts in Y and Z direction. Those are the stresses acting in plane with the PV area. The figure shows that in

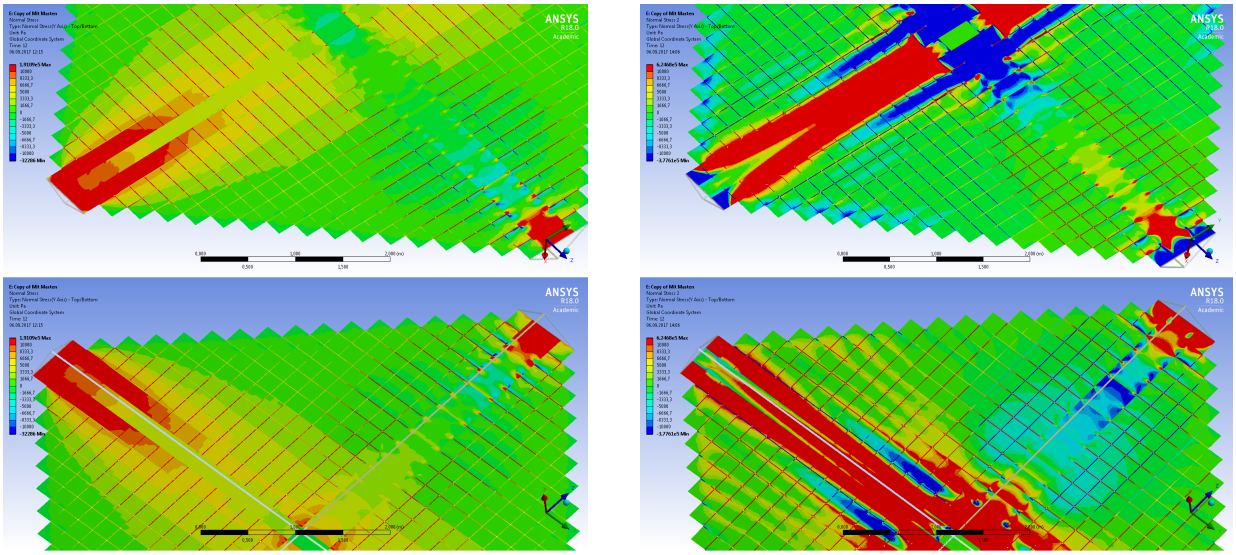

Figure 3.24: Normal stresses in Y direction of the arrays equipped the Gossamer-2 (left) and the DeOS (right) masts at a pre tensioning force of 3 N.

case of the Gossamer 2 mast nearly all of the connection elements are under tensional stress (red) in Y as well as in Z direction. This is the expected and the desired result because the tensional stress causes the increase in the eigenfrequency. In contrast, many of the connection elements of the array equipped with the DeOs mast are under compression stress (blue) on the top and under tensional stress on the bottom side of the array. Thus those connection elements are under bending stress. The reason for that is due to the high flexibility of the DeOs mast. The masts bend up very much when they are pushed outwards. At the same time the tips of a mast perform an in plane movement towards the centre of the array. This causes a loss of tension in the areas of the array near the edges. Consequently the array surface sags which causes the bending stress in the connection elements. The sagging of the PV surface can be seen in figure 3.26. This is also the reason for the low eigenfrequency and the very small increase of the eigenfrequency with increasing pre stress in

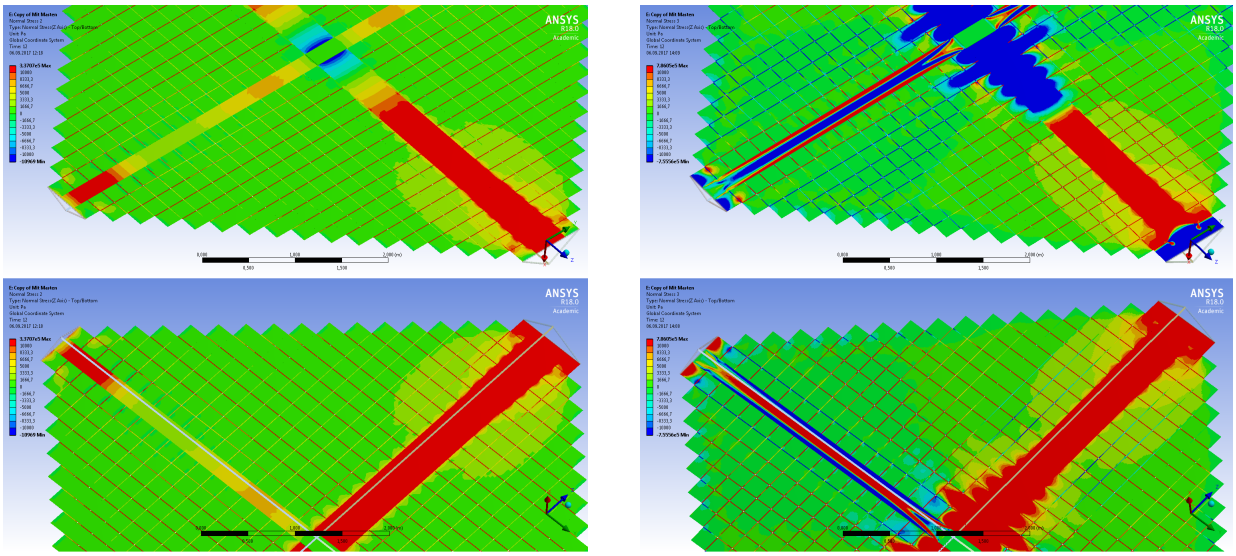

Figure 3.25: Normal stresses in Z direction of the arrays equipped the Gossamer-2 (left) and the DeOS (right) masts at a pre tensioning force of 3 N.

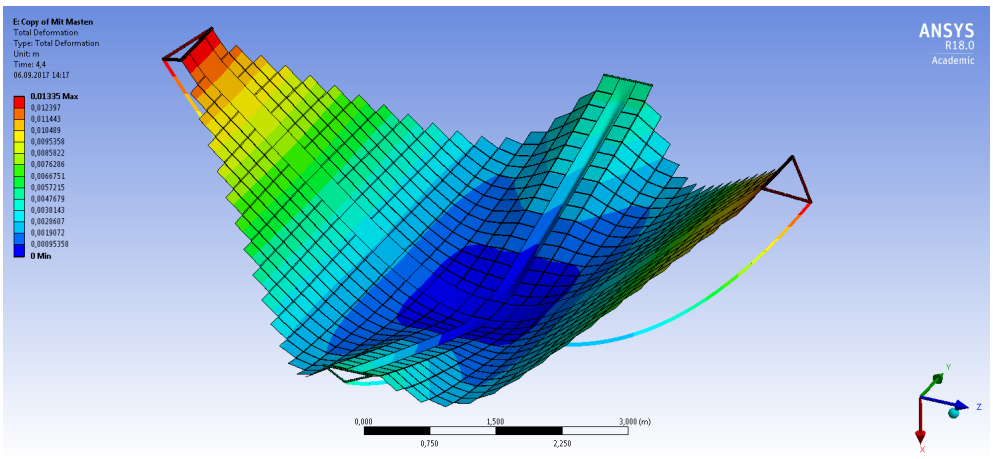

Figure 3.26: The deformation of the pre tensioned array with the DeOs mast shown with 5 x amplification.

terms of the less siff masts. While the increasing pre stress increases tensionals stress in the areas of the surface in proximity to the diagonals the up bending of the mast cause a loss of tension in the areas near the edges. Hence, the eigenfreuency does not increase significantly. This effect in comparison is much smaller in case the array is equipped with the gossamer 2 mast. To exemplify this the deformations of the masts are compared. When applying a pre tensioning force of 3 N, the maximum deflection is 42.95 mm for the DeOs mast and 1.14 mm for the Gossamer 2 mast. So when a force of 3 N is applied on the Gossamer 2 mast the up bending effect of the masts is practically negigible. With a pre tensioning force of 40 N the maximum delfection is 15.24 mm. This behaviour of the Gossamer 2 mast also explains the decrase of the eigenfrequency with a pre tensioning force of more than 17 N. At high forces the up bending of the masts cause areas with low tension which decrease the eigenfrequency. Comparing the mechanical properties of the masts the Gossamer 2 mast is the best one. It has the highest eigenfrequency and leads to a very small deformation of

the array out of plane. The modal masses of alls masts are relatively similar when a proper pre tensioning force is applied. Despite the good properties the Gossamer 2 mast is not the favourable mast. Compared to the Gossamer 1 and DeOs mast the Gossamer 2 mast is much heavier. Also a pre tensioning force of 17 N is disadvantageous because larger engines for the deployment are needed to obtain this which increases overall system weight. Additionally the masts are larger regarding the cross sectional area and consequently the deployment units are larger. Space is a major critical point of the design. Hence, the Gossamer 2 mast is not considered for the design and further analysis. The natural frequencies and the weight of the configurations with the Gossamer 1 and the DeOs mast do not considerably differ. However, the configuration with the Gossamer-1 mast has lower modal mass and is therefore selected for further analysis.

3.3.5 Static analysis

As mentioned before the Gossamer 1 mast is analyzed further. A static analysis is done considering the athmospheric drag that was calculated in section 2.2.3. The static analysis is done to obtain knowlegde about the stresses in the array in a low earth orbit and whether there may be interaction between the PV surface and the masts.

Analysis settings

For the static analysis the quarter model of the GoSolAr is used. The same boundary conditions as in the modal analysis are used. Additionally symmetry constraints are set to consider that the model is only one quarter. The array is pre tensioned but the pre tensioning force is haved because the masts in the model are also halved. So a preload force of 1.5 N is applied on each mast. Additionally a pressure of 0.001 $\frac{\mathrm{N}}{\mathrm{m}^2}$ is applied on the bottom side of the array over xxxx time steps. This pressure refers to a oribtal height of about xxxx km as visible in figure **??**.

4 Accommodation study

This chapter deals with the accommodation of the GoSolAr. The arrangement of the folded photovoltaic and the deployment units is examined. Several options are elaborated for the 5 x 5 m² technology demonstrator as well as for the full size 20 x 20 m² array. Furthermore the accommodation of the full size GoSolAr on a S/C is studied. Therefor a S/C of the size of the ATV or a geostationary satellite is taken as a reference. Advantageous arrangements are investigated with regard to the payload fairing of Ariane 5 and Vega. The accommodation study is done with the help of Catia V5.

4.1 Technology demonstrator

For the technology demonstrator the Gossamer-1 mast is taken into account as mentioned. The main advantage of this carbon fibre mast is its low weight. The main disadvantage is its large volume. Therefore additionally the 0.86" Dia High Force STEM Boom by Northrop Grumman which is much smaller in size is used for the accommodation study. A similar mast of the same size was used for the photovoltaic arrays of the Hubble Space Telescope. These arrays were also equipped with flexible photovoltaic and had a similar size as the GoSolAr technology demonstrator. Thus they are assumed to be applicable.

4.1.1 The CAD model

To investigate arrangements of the components the components are roughly drafted in Catia. In Catia V5 the photovoltaic stacks and the deployment units were designed as simple shapes of the size of the corresponding parts and assembled in different ways. The dimensions of the photovoltaic stacks were determined by the number of photovoltaic elements and their thickness as follows:

$$h = 153 \cdot 327.1\ \mu m \tag{4.1}$$

$$h = 50.046\ mm \tag{4.2}$$

For the configurations in which the main harness is folded into the PV stacks the thickness of 66 layers of harness needs to be added resulting in a thickness of:

$$h = 66 \cdot 62.1\ \mu m + 50.046\ mm \tag{4.3}$$

$$h = 54.145\ mm \tag{4.4}$$

For the technology demonstrator only configurations with the harness folded into the PV stacks are considered. Assuming a width of the harness of 200 mm an uncovered harness would increase the width by around 50 % while folding the harness into the stack its thickness only increases by approximately 4 mm. Altough in this configuration the harness needs to be twice as wide as in an uncovered configuration this still is the favourable option. The dimensions of the delpoyment unit of the Gossamer-1 mast were derived from the deployment units of the Gossamer-1 solar sail. All the redundant parts of the deployment units are left out to keep it as small as possible. Also

it is considered that two masts can be deployed in opposite directions from one unit using one spool. So two mast can be deployed from one deplyment unit. The STEM mast was drafted using a technical drawing (Grumman, 2015). It is also considered that one deployment unit can deploy 2 masts in opposite directions from one spool. Using those elements several arrangement options are developed.

4.1.2 The accommodation study of the technology demonstrator

The different design options are assessed evaluating their power per volume ratio. Power and volume are assumed as follows:

$$P = A_{PV\,generator} \cdot \eta \cdot E_0 \tag{4.5}$$

with an area of the PV generator of 0.04 m² and an efficiency of 13 %.

$$V = h \cdot b \cdot d \tag{4.6}$$

The volume is determined using a cubical space envelope for the arrangements. table 4.1 shows the dimensions and the power to volume ratio of several arrangement options. The corresponding options shown in figure 4.1. Regarding the configuration with the Gossamer-1 mast options 2 and 3 have the best power to volume ratios. In option 2 the shape of the PV generators is changed from quadratic to rectangular to fit better to the arrangement. The area and thus the power of each generator remains unchanged. These arrangements are not necessarily the best ones espacially with regard to the fact that the size of the photovoltaic stacks is very optimistic. It is assumed that the stacks may be thicker due to spacers between each PV element. In these configurations thicker PV stacks would significantly increase the volume while in the arragement 1 the volume does not increase up to a certain increase of the thickness of the PV stacks. For example comparing the options 1 and 3 an incrase of the PV stacks' thickness of 45 mm leads to a significant increase of the volume of option 3 by 32 % but does not affect the size of option 1. In this case option 1 even has a better power to volume ratio. As the values in the table show and as it is also visible in the figures the deployment units have a significant influence on the volume of the arrangement. A ratio nearly twice as high is obtained with the smaller mast than with the carbon fibre mast comparing the best option of each mast type. Regarding the configuration with the STEM masts option 2 is the best one. Again the shape of the PV generators is changed to a rectangular shape to optimize the volume. So it can e concluded that the small metal mast is advantageous in terms of space. Nevertheless the space saving has to be paid with higher weight.

	Gos-1-1	**Gos-1-2**	**Gos-1-3**	**STEM-1**	**STEM-2**
Height in mm	552	226	387	312	420
Width in mm	423	674	423	423	281
Depth in mm	237	300	280	204	204
Volume in mm^3	55338552	45697200	45836280	26923104	24076080
Power in kW	4.35	4.35	4.35	4.35	4.35
Ratio in $\frac{kW}{m^3}$	78.6	95.2	94.9	161.6	180.7

Table 4.1: Dimensions and ratios of serveral options of the technology demonstrator.

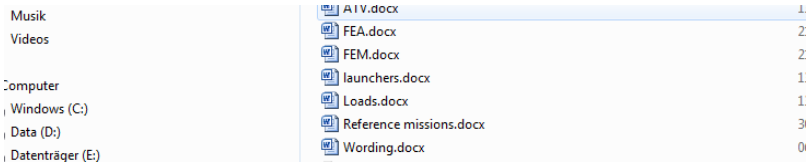

Figure 4.1: The options for the technology demonstrator corresponding to table 4.1.

4.2 Full size array

In case of the 20 x 20 m² full size array the larger Gossamer-2 mast is used in the accommodation study. As an alternative with smaller volume the 1.34" High Force STEM Drive mast by Northrop Grumman is used. The dimensions of the Gossamer-2 deployment unit are assumed comparing the size of both masts. The flattened Gossamer-2 mast is 1.935 time larger than the flattened Gossamer-1 mast. Therefore the width of the Gossamer-2 deployment unit is multiplied by this value. The other dimensions do not change that significantly because the spool diameter remains the same. The other 2 dimensions are multiplied by 1.2. The dimensions of the STEM mast are roughly derived from pictures provided on the website of Northrop Grumman. In terms of the full size array only a configuration with uncovered harness is considered. In a conifguration with the harness folded in the PV stack the harness would need to be nearly 1.7 m wide compared to 0.2 m in the uncovered configuration. The different options as well as their dimensions, power and volume are shown in table 4.2 and figure 4.2. It is again apparent that the size of the deployment unit has a large influence on the total volume of the stowed array and with that on the power to volume ratio. In terms of the carbon fibre mast the full size array's power to volume ratio is better than the technology demonstrator's. Using the small metal masts the power to volume ratio is similar in the full size coniguration compared to the technology demonstrator. In terms of the metal masts both options are similar in performance. Both options have large clearances between the PV stacks. So in case the thickness of the stacks increases the models are still applicable. Option 2 has two main disadvantages. Due to the non quadratic PV generators the deployed array has also a non quadratic shape. Additionally the main harness is longer but this disadvantage may be compensated by the shorter string harness. In terms of the CFK mast als all options are similar regarding the power to volume ratio. Option 1 has the main advantage of the PV generators being quadratic. Options 2 and 3 both have an non quadratic PV generators. Nevertheless those elongated options may be advantageous in terms of the accommodation of a S/C.

	Gos-2-1	**Gos-2-2**	**Gos-2-3**	**STEM-1**	**STEM-2**
Height in mm	836	2315	480	1006	1914
Width in mm	1871	1000	3107	1871	1000
Depth in mm	432	285	432	204	204
Volume in mm^3	675715392	659775000	644267520	383974104	390456000
Power in kW	69.6	69.6	69.6	69.6	69.6
Ratio in $\frac{kW}{m^3}$	103	105.5	108	181.3	178.3

Table 4.2: Dimensions and ratios of serveral options of the full size array.

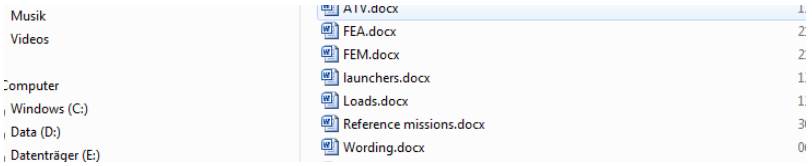

Figure 4.2: The options for the full size array corresponding to table 4.2.

4.3 Accommodation on a satellite

The payload fairing of the Vega is used to evaluate options of accommodation of the stowed PV array on a satellite. figure 4.3 shows an example on how the array with option 2 with the Gossamer-2 mast can be accommodated in a launch arrangement in a configuration with 2 PV arrays on a satellite. The satellite has a width and depth of 1400 mm · 1700 mm and a height of 2200 mm. On a slightly smaller satellite of a size of 1400 mm · 1400 mm · 2200 mm a configuration with 4 array with the STEM mast on each side wall of the satellite is possible as figure 4.4 shows. This study shows that the elongated and flat configurations which can use the spare space that is left by a cuboidal S/C in a circular payload fairing are favourable.

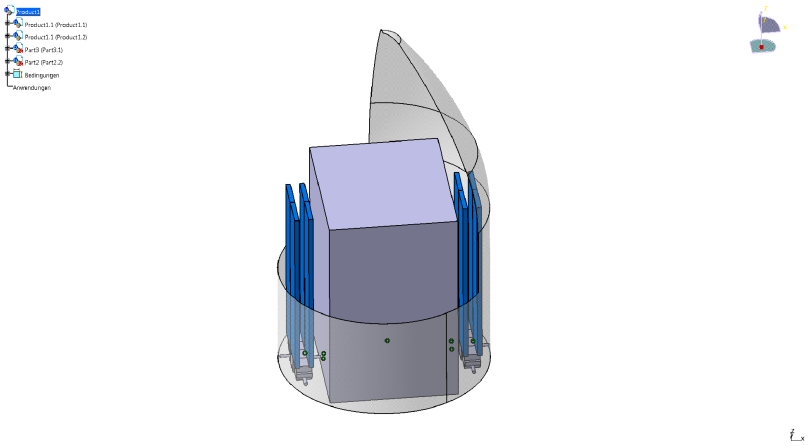

Figure 4.3: Satellite with two PV arrays inside the Vega payload fairing.

Due to the fact that the axis that connects both PV arrays must always go through the centre of gravity means need to be developed to ensure this.figure 4.5 shows a suggestion on a possible basic design. The PV stacks are brought into a horizont position by an extension of the mast that consists of two rod elements and three hinges. By this mean the PV array can be deployed more easily and it can be mounted wherever necessary on the S/C and still cover a large area of the side wall.

4.4 Accommodation on a large S/C (ATV)

An accommoadtion study of the full size array on the GoSolAr is done. A coarse model of the ATV is drafted in Catia. The PV arrays of the ATV are replaced by the full size array. figure 4.6 shows the outcome. It is visible that the required space for the GoSolAr does not significantly differ from the required space for the conventional PV arrays. On the other hand the available power differs considerably. AAmadieu and Herolet state that the ATV's photovoltaic has a power of approximately

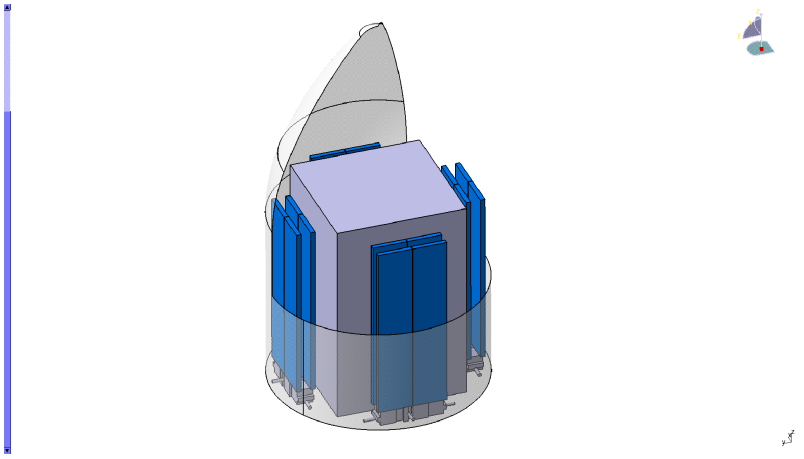

Figure 4.4: Satellite with four PV arrays inside the Vega payload fairing.

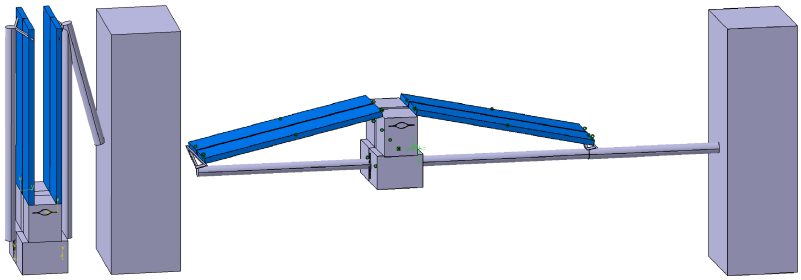

Figure 4.5: Stowed and partly deployed GoSolAr on a S/C.

3.8 kW while a power of 70 kW is assumed for each GoSolAr array resulting in a total power of 280 kW for a configuration with 4 arrays. figure 4.7 shows the ATV with the 4 deployed GoSolAr arrays.

4.5 Evaluation

The accommodation study shows that in all cases a configuration with elongated PV generators result in the best power to volume ratio. But these configuration also come with disadvantages. The deployed shape of the array is not quadratical but rhombohedral as it is also visible in figure 4.7. In the optimal configuration of the full size array using the STEM mast the diagonal increases from approximately 28 m to 64 m. Hence these configurations have higher demands for stability. The much wider array will also results in a lower eigenfrequency which is disadvantageous. This requires stiffer masts which may incease the weight of the array. The wider PV generators may also increase the complexity of the deployment.

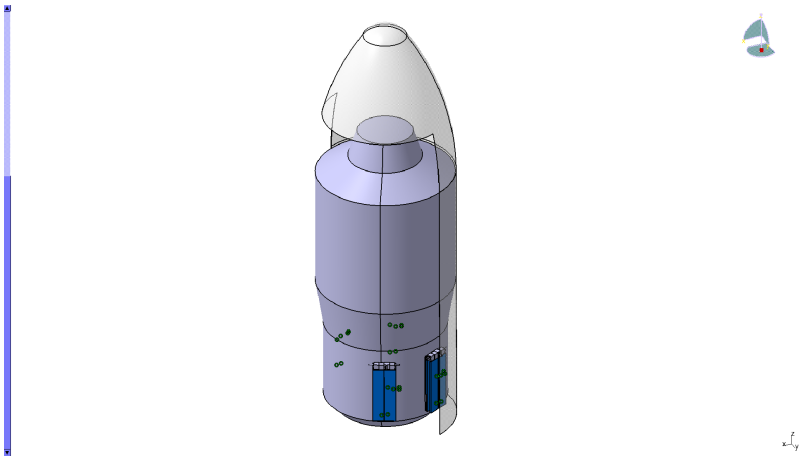

Figure 4.6: ATV with stowed GoSolAr inside the Ariane 5 payload fairing.

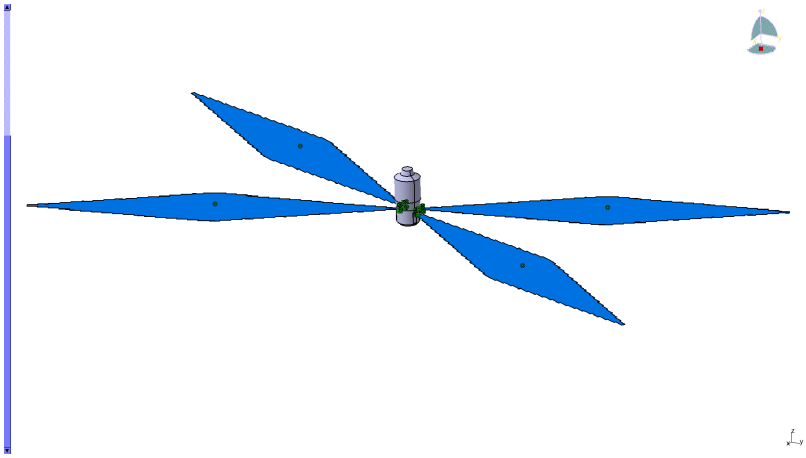

Figure 4.7: ATV with deployed GoSolAr.

Bibliography

Anthony, S., 2012. Newton-raphson-verfahren. Website, 11.09.2017.
URL https://www.extremetech.com/extreme/144296-nasas-next-ion-drive-breaks-world-record

Arianespace, E. P., 2014. Vega User's Manual Issue 4 Revision 0, 0th Edition. Vol. 4. Arianespace.

Arianespace, R. L., 2016. Ariane 5 User's Manual Issue 5 Revision 2, 2nd Edition. Vol. 5. Arianespace.

Banik, J. A., 2014. Structural scaling metrics for tensioned-blanket space systems. Ph.D. thesis, The University of New Mexico, Albuquerque, New Mexico.

Bol, P. D.-I. M., Bolea Albero, D.-I. A., 2016. Anwendung kommerzieller fe-software thema 1: Einfuhrung in fem und abaqus. Presentation.

CAE-Wiki, 2015. Newton-raphson-verfahren. Website, 11.09.2017.
URL https://www.nasa.gov/centers/glenn/about/fs21grc.html

DLR-homepage, 2017. Europa nimmt kurs auf die iss. Website, 08.09.2017.
URL http://www.dlr.de/dlr/desktopdefault.aspx/tabid-10369/563_read-478/#/gallery/14056

ESA-homepage, n.d.a. Die versionen der ariane 5. Website, 08.09.2017.
URL http://www.esa.int/ger/ESA_in_your_country/Germany/Die_Versionen_der_Ariane_5

ESA-homepage, n.d.b. Maßgeschneidert: Die ariane 5 es. Website, 08.09.2017.
URL http://www.esa.int/ger/ESA_in_your_country/Germany/5._Massgeschneidert_Die_Ariane_5_ES/

Foster, J. E., Haag, T., Patternson, M., Williams jr., G. J., Sovey, J. S., Carpenter, C., Kamhawi, H., Malone, S., Elliot, F., 2004. The high power electric propulsion (hipep) ion thruster.

Gebhardt, C., 2014. Praxisbuch FEM mir ANSYS Workbench, 2nd Edition. Vol. 1. Hanser Verlag, Munchen.

Grumman, N., 2015. Storable tubular extendable member. Website, 11.09.2017.
URL http://www.northropgrumman.com/BusinessVentures/AstroAerospace/Products/Pages/STEM.aspx

NASA-homepage, 2016. How does an ion thruster work? Website, 08.09.2017.
URL https://www.nasa.gov/centers/glenn/about/fs21grc.html

Seefeldt, P., 2017. Development and qualification of deployable mambranes for space applications. Ph.D. thesis, Universitat Bremen, Bremen, unpusblished Draft.

Tipler, P. A., 2000. Physik, 1st Edition. Vol. 1. Spektrum Akademischer Verlag, Heidelberg, Berlin, Oxford.

List of Figures

List of Tables

List of symbols

Symbols and indecies

A	Area	m
b	Width	m
c_l	Speed of light in the vacuum, $c = 299.792.458\ \frac{m}{s}$	$\frac{m}{s}$
c_D	Drag coefficient	
a	aaaaaa	
c_p	Pressure coefficient	
c_s	Speed of sound	$\frac{m}{s}$
d	Depth	m
E	Energy	J
E_0	Solar constant, $E_0 = 1367\ \frac{W}{m^2}$	$\frac{W}{m^2}$
F	Force	N
g	Erdbeschleunigung	$\frac{m}{s^2}$
h	Height	m
I	Intensity	*weissnicht*
k	Stiffness	$\frac{N}{m}$
l	length	m
m	Mass	kg
p_D	Drag pressure	$\frac{N}{m}2$
p_s	Solar radiation pressure	$\frac{N}{m}2$
t	Time	s
u	Displacement	m
V	Volume	m
v	Velocity	$\frac{m}{s}$
P	Impluse	W
W	Energy of a wave	J
Y	Young's modulus	$\frac{N}{m}2$
α	Angle of inclination	
δ	Difference	
δt	Time step	$\frac{rad}{s}$
η	Efficiency	
μ	nochmal nachgucken	
ω	ω,	$\frac{rad}{s}$
π	$\pi, \pi = 3.14$	

ρ	Density	kg/m^3

crit	Critical
max	Maximalwert
min	Minimalwert

Abbreviations

ATV	Automated Transfer Vehicle
AVUM	Attitude & Vernier UpperModule
CIGS	Copper indium gallium selenide
DeOs	De-Orbit Sail
DLR	Deutsches Zentrum für Luft- und Raumfahrt
FE	Finite element
FEA	Finite element analysis
FEM	Finite element method
GRC	Glenn Research Center
GTO	Geostationary transfer orbit
HiPEP	High Power Electric Propulsion Program
HTPB	Hydroxyl-Terminated Poly Butadiene
IfR	Institut für Raumfahrtsysteme
ISS	International Space Station
L/V	Launch vehicle
LEO	Low earth orbit
NASA	National Aeronautics and Space Administration
NTO	Nitrogen Tetroxide
PV	Photovoltaic
S/C	Spacecraft
SRM	Solid Rocket Motor
STEM	Storable Extendible Tubular Member
SYLDA5	Système de Lancement Double Ariane 5
UDMH	Unsymmetrical Dimethylhydrazine

VESPA Vega Secondary Payload Adapter